The Planetary Science Journal, 5:275 (17pp), 2024 December https://doi.org/10.3847/PSJ/ad8fac


# Deriving the $N_2$–CO Binary Phase Diagram Using Experimental Techniques and Thermodynamics

Shaelyn M. Raposa[1,2,6], Sugata P. Tan[3], William M. Grundy[1,2], Jordan K. Steckloff[3,4], Jennifer Hanley[1,2], Stephen C. Tegler[1], Anna E. Engle[1,2], Cecilia L. Thieberger[1,2], and Gerrick E. Lindberg[5]
[1] Department of Astronomy and Planetary Science, Northern Arizona University, Flagstaff, AZ 86011, USA
[2] Lowell Observatory, Flagstaff, AZ 86001, USA
[3] Planetary Science Institute, Tucson, AZ 85719, USA
[4] University of Texas at Austin, Austin, TX 78705, USA
[5] Department of Chemistry and Biochemistry, Northern Arizona University, Flagstaff, AZ 86011, USA
*Received 2024 February 9; revised 2024 October 15; accepted 2024 October 24; published 2024 December 18*

## Abstract

In the distant outer solar system, carbon monoxide (CO) and nitrogen ($N_2$) ices tend to be colocated in the same deposits due to their similar molecular weights and sublimation properties. For instance, these volatiles are abundant on the surfaces of Pluto and Triton, so knowledge of their phase behavior is necessary for understanding surface evolution and geology. However, it is presently unclear how mixing between CO and $N_2$ molecules affects the physical properties of such mixtures. Here, we measured the liquidus, solidus, and alpha–beta phase transitions for the $N_2$ and CO binary system. We observed the liquidus by using visual inspection. The solidus and alpha–beta transitions were measured by using Raman spectroscopy. The laboratory results were later compared to a thermodynamic model, CRYOCHEM 2.0. The liquidus and solidus were consistent with CRYOCHEM 2.0. However, the alpha–beta coexistence region is shown to be narrower in the laboratory results than in the thermodynamic model. Finally, we present a method for deriving the compositions of a sample using Raman spectroscopy (Appendices A.1 and A.2).

*Unified Astronomy Thesaurus concepts:* Kuiper Belt (893); Ice phases (2273); Pluto (1267); Triton (2187); Experimental techniques (2078); Vibrational spectroscopy (2249); Spectroscopy (1558)

*Materials only available in the online version of record: data behind figures*

## 1. Introduction

In the outer solar system, ternary mixtures of nitrogen ($N_2$), methane ($CH_4$), and carbon monoxide (CO) play an important role in the evolution of planetary surfaces. Specifically, this mixture dominates the surface and atmospheric processes on Pluto. The redistribution of these mobile volatiles has carved out Pluto's landscape over time, creating glaciers and valleys (J. M. Moore & A. D. Howard 2021). One notable region where this mixture resides in large quantities is Sputnik Planitia, a vast glacial region dominated by $N_2$-rich ice, with smaller amounts of CO- and $CH_4$-rich ices (W. M. Grundy et al. 2016; S. Protopapa et al. 2017; B. Schmitt et al. 2017). Additionally, such ternary mixtures can be found on the icy surface of Neptune's largest moon, Triton (E. Quirico et al. 1999).

Since mobile volatiles such as these play such a crucial role in the evolution of a planetary surface, it is important to understand the interactions and phase behaviors of these mixtures. One way that we can represent these behaviors is through phase diagrams. Phase diagrams show what phases are present for a mixture as a function of temperature, pressure, and composition. However, the literature is limited in fully mapped phase diagrams for such materials at the low pressures and cryogenic temperatures relevant to Pluto and Triton. S. M. Raposa et al. (2022) started to fill in these literature gaps by first mapping the three-phase solid–liquid–vapor (SLV) curves for the $N_2$–CO, $N_2$–$CH_4$, and CO–$CH_4$ binary systems. Here, we continue studies of these materials by creating the full $N_2$–CO binary phase diagram using a low-pressure manometer and Raman spectroscopy to study where phase changes occur for various compositions. This binary mixture is of interest since, on both Pluto and Triton, the presence of CO generally correlates well with that of $N_2$. On Pluto, both have strong signatures in Sputnik Planitia and the 40°–60° latitude band in the northwest region (Figures 15 and 24 in B. Schmitt et al. 2017), and on Triton, $N_2$ and CO are more commonly found to be intimately mixed, rather than existing as separate ices on the surface (S. C. Tegler et al. 2019).

Investigations of this binary were first conducted in the 1930s by T. T. H. Verschoyle (1931) and then M. Ruhemann et al. (1935). It is well known that solids of $N_2$ and CO are isomorphous with each other (R. J. Loveland et al. 1972) where they exist in hexagonal crystalline structure at high temperatures (beta phase) and cubic structure at lower temperatures (alpha phase). By visual observation, Verschoyle measured the freezing points on the liquidus at four compositions with a likely inflection point on the pressure–temperature ($P$–$T$) diagram (T. T. H. Verschoyle 1931). However, melting points on the solidus were not measurable, though they were believed to be close to the liquidus. The phase-coexistence region sandwiched by the liquidus and solidus was later found calorimetrically to be extremely narrow (M. Ruhemann et al. 1935), as the composition of liquid and beta-solid phase was

[6] Corresponding author.

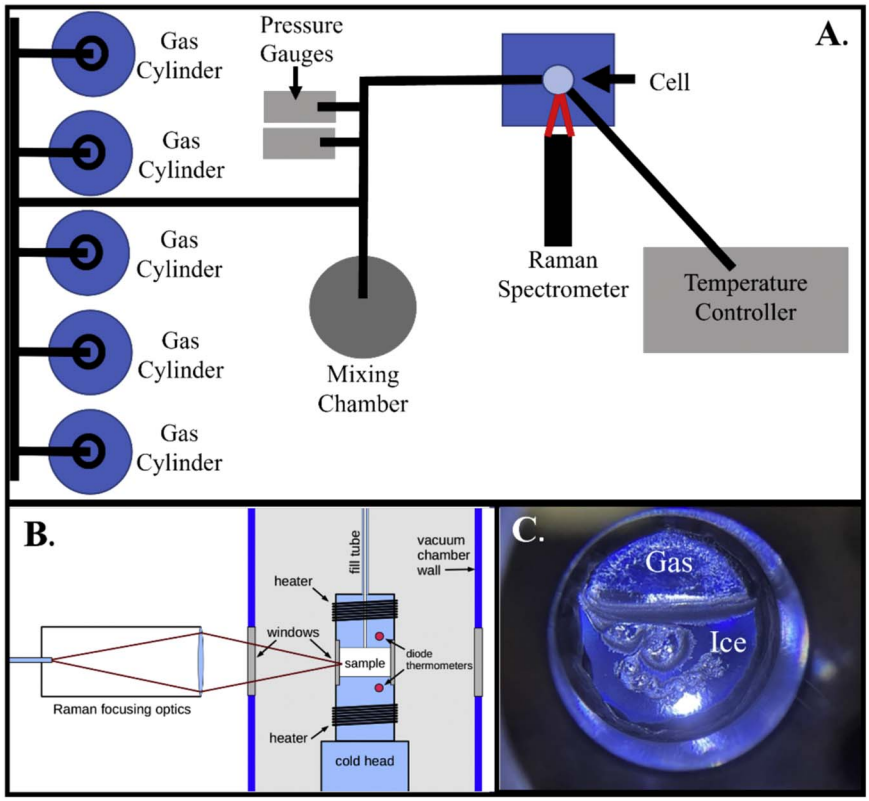


**Figure 1.** (A) Top view and (B) side view of the laboratory setup. (C) Example picture of the sample cell during an experiment. For scale, the sample volume is 20 mm long and 15 mm in diameter. In this case, the cell contains $N_2$–CO. (Note: the blue appearance is caused by antireflection coating on the Raman's focusing optics behind the cell and is not the actual color of the cell and its contents.)

always slightly different. This was also the case for the solid–solid (SS) transition at lower temperatures (M. Ruhemann et al. 1935). Moreover, like the solidus, the lower SS boundary was not obtained with certainty. Because calorimetric specific-heat measurements require hours for equilibration, which potentially introduced inaccuracies, M. J. Angwin & J. Wasserman (1966) repeated Ruhemann's SS measurements, but the phase transitions were determined by X-ray diffraction for eight compositions along the alpha–beta phase boundary curves. These compositions were mixed in the gas phase, condensed to a liquid, and frozen in a copper cell. Contrary to Ruhemann's work, it is stated that equilibrium was reached during these experiments. They indicated that the lattices of $N_2$ and CO may not be quite identical at low temperatures, so that the mixture does not show an ideal lens-shaped phase-coexistence region, thus producing an asymmetrical phase diagram, which contradicted the results of M. Ruhemann et al. (1935).

M. Vetter et al. (2007) later applied IR spectroscopy to reproduce the phase diagrams (both SL (solid–liquid) and SS). For the first time, thermal hysteresis was discussed, where the warming cycle was deemed more reliable due to supercooling effects in the cooling cycle. The phase-coexistence region was about 2 K wide at a 0.59 mole fraction of $N_2$. Similar to M. Vetter et al. (2007), we use vibrational spectroscopy, more specifically, Raman spectroscopy, to assess the phase diagram while also accounting for supercooling effects on the mixtures. While both IR and Raman spectroscopies as described here probe transitions between vibrational states of molecules, their differing underlying physical mechanisms present different advantages. In IR spectroscopy, a vibration is active if there is a permanent dipole that changes with the vibration. In Raman spectroscopy, a vibration is active if the polarizability of the molecule along the vibration allows for an induced dipole to form. The implications of these mechanisms are clear if they are considered for homonuclear and heteronuclear diatomic molecules, like $N_2$ and CO. Homonuclear diatomic molecules are therefore not IR-active, while they are Raman-active. While some transitions might be strictly forbidden in the ideal case, the transition can be observed due to asymmetries arising from the local molecular environment (for example, weak IR absorption by $N_2$). Raman spectroscopy is thus useful for probing the molecular environment (e.g., C. Turc et al. 1992). Furthermore, the setup of our scattering Raman spectrometer is more amenable than transmission spectroscopy, which requires the spectrometer beam to pass through the sample unscattered. Therefore, Raman spectroscopy presents several advantages over IR spectroscopy for our study.

In this paper, we first describe the experimental setup and the process for mixing samples. Next, we discuss how to use the Raman spectra to derive where phase boundaries are located. Then, we present our $N_2$–CO binary phase diagram and discuss how it compares to a thermodynamic model, CRYOCHEM 2.0, the literature previously described, and what implications the results could have for places like Pluto and Triton.

## 2. Methods

### 2.1. Experimental Setup and Sample Mixing

The experiments described in this paper were performed in the Astrophysical Materials Laboratory at Northern Arizona University. A more detailed description of the laboratory setup can be found in previous publications (e.g., W. M. Grundy

et al. 2011; S. C. Tegler et al. 2010, 2012, 2019; C. J. Ahrens et al. 2018; A. E. Engle et al. 2021). Figure 1(A) provides an overhead view of the setup. Gas cylinders are hooked up to stainless steel tubing that leads to the mixing chamber. A sample may be premixed in the gas phase in the chamber prior to injection into the sample cell (Figure 1(C) shows the sample cell with an ice $N_2$–CO mixture inside). The sample cell is a 20 mm long, 15 mm diameter cylindrical volume composed of aluminum alloy and enclosed using sapphire windows pressed up to indium wire gaskets. As shown in Figures 1(B) and (C), the sample can be viewed by eye from one side and is probed by a Kaiser Rxn1 Raman system on the other side. Though the side of the cell viewable by eye is exposed to ambient room light, it is covered with an aluminum foil cap while spectra are taken so that the spectra are not affected by this light in the visible-light wavelength range. The Raman may be moved on all three axes to probe any part of the sample. It has a laser wavelength of 785 nm, or 12,739 $cm^{-1}$, and the measured wavelength range of the Raman shifts is 100–3425 $cm^{-1}$, with a resolution of 2 $cm^{-1}$. In this work, an exposure time of 3 s is frequently used. The Raman spectrometer is used in these experiments for measuring compositions and phase transitions of the sample (described more in Appendices A.1 and A.2 and Section 2.2, respectively).

This setup can reach temperatures as low as 30 K, making it ideal for studies of outer solar system planetary bodies. Prior to the start of an experiment, the sample cell must be cooled to the desired start temperature. This is generally a temperature just above the freezing point of the sample used that day. For $N_2$–CO mixtures, this will be around 64–68 K. The cell is cooled by a two-stage CTI 1050 closed-cycle helium refrigerator, and the temperature is controlled by a Lakeshore Model 335 temperature controller that monitors a pair of DT-670 silicon diode thermometers above/below the cell. Two Lakeshore WNC-32 nichrome heaters (with composition 80% nickel, 20% chromium) are also placed above/below the cell. In these experiments, we control the temperature using the bottom heater, thus cooling the sample from below. This creates a small vertical thermal gradient throughout the cell of about a few tenths of a kelvin, which is less than if the top heater was used. We report estimated measurement errors not larger than ±0.5 K, which includes both random and potential systematic uncertainties. We performed temperature calibration tests using pure $N_2$, CO, and $CH_4$ in equilibrium at their triple points (63.15 K, 68.0 K, and 90.7 K, respectively). Temperature offsets between DT-670 diode readings and the known phase change temperatures were corrected using a linear correction fitted to the measured triple-point temperatures of $N_2$, CO, and $CH_4$, plus measurements of the temperatures of the $N_2$ and CO alpha–beta ice phase transitions known to occur at 35.61 K and 61.6 K, respectively (C. S. Barrett & L. Meyer 1965; T. A. Scott 1976).

This system contains two vacuum systems (one for the mixing area and cell and one for the vacuum chamber). Large volumes of material are removed from the mixing area and cell using a Varian/Agilent DS302 rotary vane roughing pump. After the bulk of the material is removed, a TV 302 turbo pump backed by a second roughing pump evacuates anything remaining. Pressure is monitored near the mixing volumes using a pair of MKS Baratron model 627 F heated capacitance manometers. One is sensitive to the range 666.6–666,611.8 Pa, and the other is ideal for monitoring lower pressures, in the range of 1.3–1333.2 Pa. The low-pressure measurements enable us to construct the *P–T* phase diagram of the three-phase solid–solid–vapor (SSV) equilibrium of $N_2$–CO for the first time; however, caution is advisable with pressures measured in the Knudsen flow regime. The cell and cold head are thermally insulated by a stainless steel vacuum cylinder and sapphire windows, keeping contaminants from condensing onto the exterior of the cell when it is cold. This region is kept at a base pressure of $\sim 1.3 \times 10^{-6}$ Pa ($\sim 1.3 \times 10^{-7}$ when the system is cold) by a TwisTorr 304 FS turbo pump and a roughing pump.

The composition to be used for an experiment is mixed by using pressures, which is pretty accurate in the range of pressures used. For example, if the desired composition for an experiment is 50% $N_2$ and 50% CO, then 33,330.6 Pa of $N_2$ gas is injected into the mixing chamber first. Then, the mixing chamber is closed off, the $N_2$ gas in the tubing leading up to the mixing chamber is pumped out, and CO gas is flushed through a couple of times to be sure that any excess $N_2$ has been evacuated. Then, we add CO to the mixing chamber with the $N_2$ until the pressure monitor reads a total pressure of 66,661.2 Pa. This mixing method is an approximate determination of the composition since we need to account for fractionation. Not all of the premixed material will make it into the cell, and the less volatile substance may preferentially condense into the fill tube. $N_2$ and CO have similar volatilities, so the effect on composition from fractionation is likely small. Nonetheless, we are not concerned with this effect since the precise factual composition of the condensed sample can be calculated during various steps of the experiment using the Raman composition derivation method (outlined in Appendices A.1 and A.2). Pressures are reported with a precision of ±0.25% of the measured pressure. Finally, after mixing the sample, the gas is injected into the cell and condensed into liquid with a gas phase above, and now the experiment may begin. Throughout the experiment, the composition may change slightly due to some gas condensing in during cooling sequences or some of the sample evaporating out when warming. This may change the sample by up to ∼2%–3% throughout an experiment, making it even more important to continuously check the true composition at various temperature steps.

### 2.2. Tracking Phase Transitions

Once the sample is condensed into the cell, it is cooled until the freezing point of the mixture (or liquidus) is reached. Near phase transitions, smaller temperature steps of ∼0.2 K were taken to improve temperature resolution. At each temperature step, a Raman spectrum is taken. Phase transitions were observed by using both visual inspection and Raman spectroscopy. Figure 2(A) shows an example of an 88% CO, 12% $N_2$ sample before reaching the liquidus, when it is still completely liquid. Figure 2(B) shows the freezing point of this mixture (liquidus). Visual inspection is used to determine the liquidus since, in some cases, the ice might not initially be in the line of sight of the Raman spectrometer, making visual inspection more accurate. Thus, the liquidus is noted as when the first sign of ice appears in the sample. Figure 2(C) shows the sample right before the melting point (solidus).

After reaching the liquidus, small temperature steps continue until the solidus (the last point where any liquid remains in the sample before transitioning completely to ice). At this point, Raman spectroscopy is used to determine the rest of the phase transitions. Previous works have shown the effectiveness of

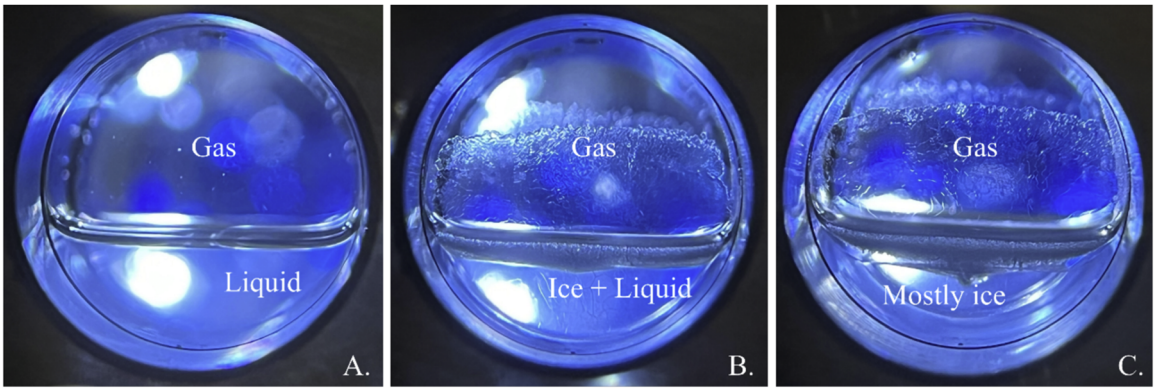


**Figure 2.** (A) Liquid in equilibrium with its vapor prior to cooling, (B) first sign of ice at freezing point (liquidus) for an 88% CO, 12% $N_2$ mole fraction mixture, and (C) vanishing liquid just above the melting point (solidus).

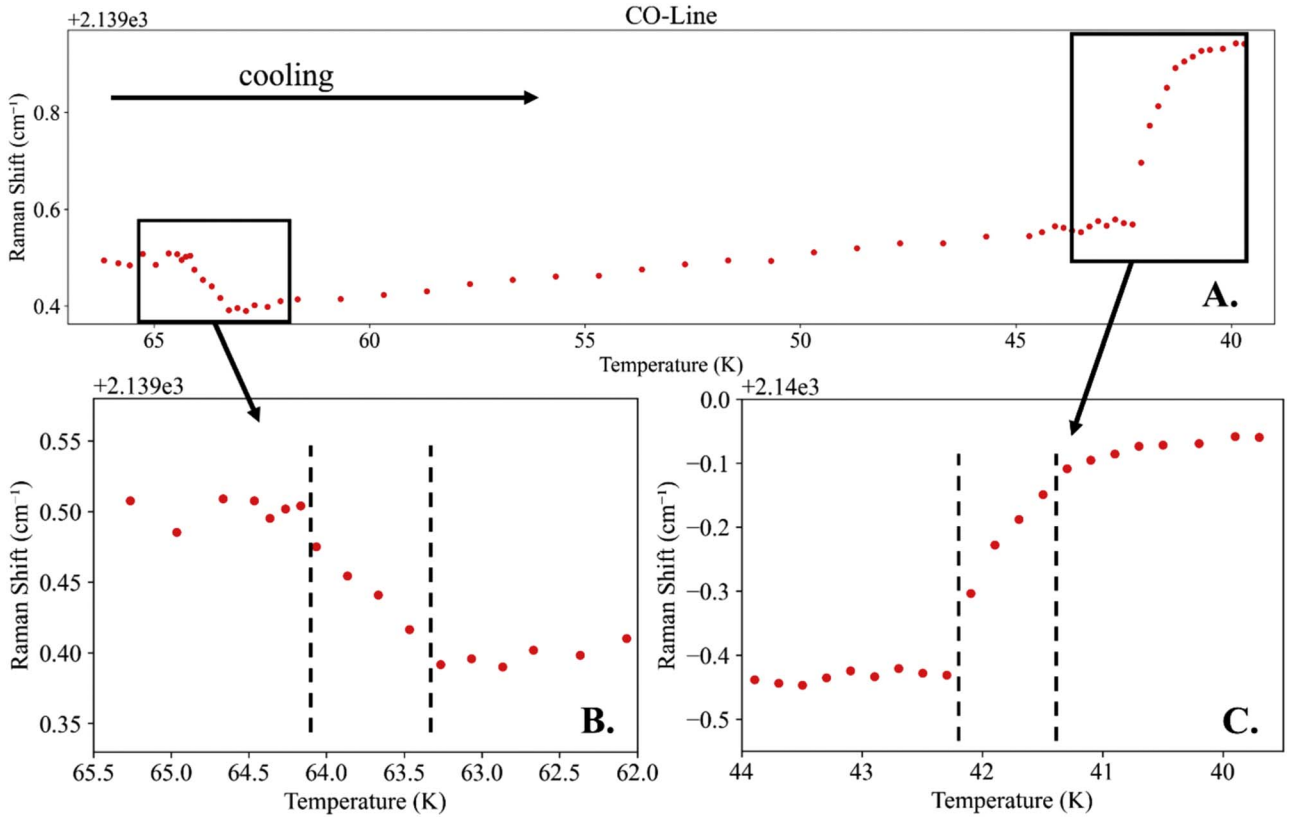


**Figure 3.** (A) Tracking the centroids of the CO line over time for a 22% CO, 78% $N_2$ mole fraction mixture. This plot is zoomed in, and the liquidus/solidus transitions are shown in (B), with the $\alpha$–$\beta$ transition shown in (C). The black dashed lines show the locations of the phase transitions for this mixture.
(The data used to create this figure are available in the online article.)

using spectroscopy to monitor phase transitions (e.g., G. Pangilinan et al. 1989). For instance, M. Vetter et. al (2007) demonstrated this by using FTIR spectroscopy for $N_2$–CO mixtures, while C. Turc et al. (1992) investigated the system using Raman, both by looking at how the frequency and width of the bands change with temperature. When a sample undergoes a phase transition, the molecular environment changes, shifting the bands slightly. Though our work uses Raman spectroscopy rather than FTIR, the same principles apply. Figure A1 in the Appendix shows examples of several background-subtracted Raman spectra for compositions of 26%, 52%, and 76% CO, cropped to the peaks of CO (Figure A1(A)) and $N_2$ (Figure A1(B)). An effective way to monitor these phase transitions is by tracking the centroids (center of mass of the band complex) of the peaks as a function of temperature (Equation (1)):

$$\text{centroid} = \frac{\sum x_i y_i}{\sum y_i}, \tag{1}$$

where $x_i$ is the Raman shift in $\text{cm}^{-1}$ and $y_i$ is the spectrum intensity (in arbitrary units). This gives the centroid in units of Raman shift ($\text{cm}^{-1}$). Plotting the locations of these centroids versus temperature results in a plot like Figure 3(A), which shows the centroids at each temperature for the 22% CO, 78% $N_2$ mixture, in this case using the CO line. Starting at the left-hand side of this figure, the first sharp change in the Raman occurs at ~64.2 K. This is the liquidus. Each sharp change

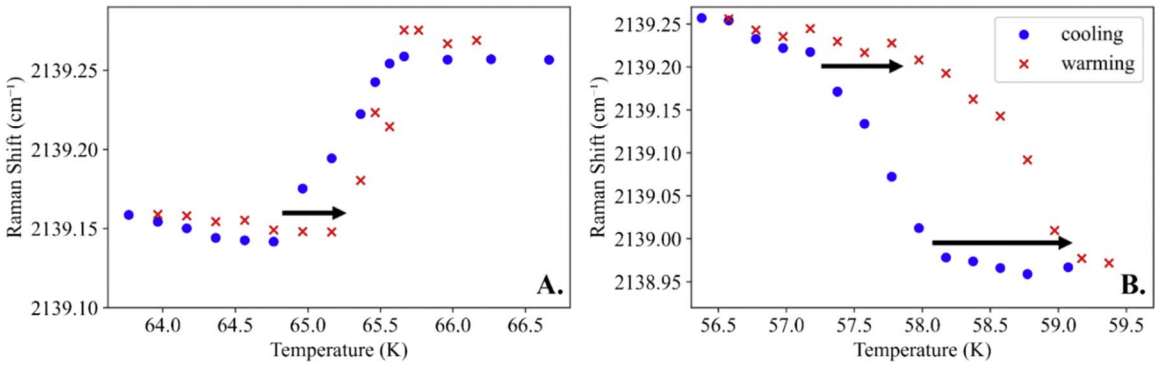


**Figure 4.** Tracking the centroids of the CO line over time for cooling (blue scatter points) and warming (red crosses) sequences for (A) the liquidus/solidus transitions of a ∼51% CO, 49% $N_2$ mixture and (B) the alpha–beta transitions of an ∼86% CO, 14% $N_2$ mixture. Arrows indicate how much the solidus and alpha–beta transitions shifted upward on the warming sequence.

(The data used to create this figure are available in the online article.)

represents when the Raman detected a change in the sample, or a phase transition. The second change occurs at ∼63.4 K. This is the solidus. Figure 3(B) shows a zoomed-in view of the liquidus and solidus Raman transitions, with the black dashed lines showing where the exact transitions occurred. Again, the liquidus is marked using visual inspection, but the solidus would be marked at the black dashed line at ∼63.4 K. The Raman shift may drift slightly during this cooling process between phase transitions. This is caused by a change in energy as the local molecular environment changes while cooling. Though the energy may change, we assume that the integrated area of the Raman bands does not because the cross section of the molecules does not change.

For this binary system, the next transition is the change from the $\beta$-phase to the $\alpha$-phase. The $\beta$-phase is an orientationally disordered hexagonal crystal structure, and the $\alpha$-phase is an orientationally ordered cubic structure (G. E. Ewing 1962; T. A. Scott 1976 and references therein). Figure 3(C) shows a zoomed-in view of these transitions. In this mixture, the transition from $\beta$ to $\alpha+\beta$ ice occurs around 42.1 K. Shortly after, the sample transitions from $\alpha+\beta$ ice to completely $\alpha$ ice at ∼41.4 K. The exact compositions at each of these phase transition points are later derived using the Raman composition derivation method (Appendices A.1 and A.2). The locations of the phase transitions are collected and added to a plot of temperature versus mole fraction, shown later in Section 3. For this phase transition, the sample appearance on cooling just before the upper phase boundary, between phase boundaries, and right after the lower phase boundary is given in Appendix A.3 for both CO-rich and $N_2$-rich compositions.

### 2.3. Accounting for Supercooling Effects

In fact, in solidification, solutions are almost never in an equilibrium state because cooling processes are usually too fast to allow enough time for complete diffusion of heat and/or solute, thus leading to departures from equilibrium conditions. A similar situation also occurs in the SS transformation, where composition gradients may result as solute diffusion is much slower than thermal diffusion (J. A. Dantzig & M. Rappaz 2009). Therefore, upon cooling, a phase change is usually observed to occur at cooler temperatures than would be expected from equilibrium thermodynamics. Supercooling can result from kinetic delays in nucleating the crystal structure of the lower temperature phase. In this work, we conducted 10 experiments, five for the liquidus/solidus phase transitions and five for the alpha–beta transitions. These experiments were roughly evenly spaced in composition. For the liquidus/solidus experiments, five compositions were cooled using the same methodology as the cooling experiments described in the previous section. After passing through the solidus, small warming temperature steps of 0.1–0.2 K were taken until passing back through the liquidus. At each warming temperature step, the sample was held for ∼10–15 minutes to allow the sample to stabilize. Figure 4(A) shows an example of one of these liquidus/solidus experiments, using the same centroid tracking method described in the last section. This experiment used a composition of ∼51% CO, 49% $N_2$. The blue scatter points show the cooling sequence, and the red crosses show the warming sequence. The liquidus is shown to occur at the same place on warming and cooling (65.6 K). However, the solidus transition is 0.4 K warmer on the warming sequence (shifts from 64.8 to 65.2 K). Both of these trends were consistent throughout the five experiments. Thus, the liquidus data remain unchanged, while the solidus data were shifted up 0.4 K to account for supercooling effects on the sample. Though this shift of 0.4 K is within our ±0.5 K temperature uncertainty error bar, that uncertainty mainly accounts for uncertainties in absolute temperature calibration. However, changes in the relative temperature can be detected to a much higher precision, better than ±0.05 K, so a 0.4 K shift can be easily observed.

Five similar experiments were conducted on the alpha–beta phase transitions. For these five experiments, CO mole fractions of 0.15, 0.32, 0.54, 0.68, and 0.86 were used. Figure 4(B) shows an example of one of these experiments. In this case, this experiment used a sample with ∼86% CO and 14% $N_2$. Temperature steps of 0.2 K were taken for these experiments. For this composition, both the transition from the $\beta$-phase to $\alpha+\beta$ and the later transition from $\alpha+\beta$ to the $\alpha$-phase occurred 1 K warmer on the warming sequence. For all of these experiments, the upper and lower $\alpha$–$\beta$ phase transitions appeared to occur 0.4–1.0 K warmer during the warming sequences. However, contrary to the liquidus/solidus experiments, the curves did not all shift by the same exact temperature amount. Therefore, since the data could not all be shifted by the same number, we decided to only use our warming data points for the $\alpha$–$\beta$ curves when making the final phase diagram, rather than using any data from the initial experiments where we were only cooling the mixtures.

**Table 1**
Fits to Experimental Data (To Be Used in Equation (2) to Get Temperature Values)

| | Liquidus | Solidus | $\beta \rightarrow \alpha+\beta$ | $\alpha+\beta \rightarrow \alpha$ |
|---|---|---|---|---|
| $a$ | 63.174 (63.101–63.248) | 63.187 (63.047–63.327) | 35.442 (34.686–36.199) | 35.704 (35.033–36.375) |
| $b$ | 5.036 (4.950–5.122) | 5.004 (4.839–5.168) | 26.429 (25.521–27.337) | 26.005 (25.203–26.808) |
| $c$ | −1.628 (−1.955– −1.301) | −3.189 (−3.815– −2.564) | 5.600 (2.127–9.072) | 0.837 (−2.222–3.896) |
| $R$-square | 0.9987 | 0.9953 | 0.9991 | 0.9993 |

**Note.** The 95% confidence intervals are listed below the values in parentheses, with the $R$-square of the fit for each curve listed in the bottom line.

It is important to note that for these experiments, the pressures were accurate during the cooling sequence, but when we started to warm back up, the pressures appeared to stick at the pressure of the final cooling step and would stay at this pressure during the whole warming sequence. We hypothesized that this was due to CO ice clogging in the fill tube and affecting our pressure readings. Therefore, we did a few more supercooling checks in which, rather than premixing in the mixing chamber, pure CO was injected directly into the cell above its freezing point. Then, $N_2$ was injected on top of it. When using this new mixing method, we used the same strategy as the previous 10 experiments. The result is that the data were still consistent in terms of where the phase transitions happened on warming and cooling. Therefore, only the pressures cannot be used in the original 10 experiments, but the phase boundary temperatures are reproducible. As the effects on pressure measurements due to clogging were eliminated using this new mixing method, pressures reported later in Figure 7 are accurate. This issue does not affect our derived compositions since, even if CO clogged in the fill tube, we derive our compositions from the Raman measurements taken throughout the experiment.

### 2.4. Polynomial Fits

We fit the experimental results for phase boundary locations to simple polynomials to enable more widespread use of our results. A linear fit would represent an ideal mixture, in which the molecules are noninteracting. However, our results demonstrate significant deviations requiring an extra, nonlinear term. We use a polynomial of the form of Equation (2),

$$T = a + bx_{\mathrm{CO}} + cx_{\mathrm{CO}}x_{\mathrm{N_2}}, \tag{2}$$

for our fits, where $a$, $b$, and $c$ are constants. Fits are listed in Table 1. The constants $a$ and $b$ describe the result of a linear fit, with constant $c$ describing the deviation from linearity, which depends on the strength of the interactions between molecular species relative to the interaction strength between molecules of the same species.

### 2.5. Thermodynamic Modeling

As the cooling experiments start from two-phase vapor–liquid equilibrium (Figure 2(a)), the freezing point at the liquidus is where the solid phase appears for the first time (Figure 2(b)), thus in a three-phase SLV equilibrium. In this equilibrium, the chemical potential of each component $i$ of the mixture, or equivalently, its fugacity, is the same in all phases,

$$f_i^{\mathrm{S}}(T, P, q) = f_i^{\mathrm{L}}(T, P, \mathrm{x}) = f_i^{\mathrm{V}}(T, P, y)\ i = 1, 2, \tag{3}$$

where the superscripts S, L, and V denote solid, liquid, and vapor, respectively. These fugacities are the properties that need to be calculated using an equation of state (EOS) at specified temperature ($T$), pressure ($P$), and the corresponding phase compositions, expressed in mole fractions, i.e., $q = \{q_i\}$ in solid, $x = \{x_i\}$ in liquid, and $y = \{y_i\}$ in vapor. As in our previous work (S. M. Raposa et al. 2022), we use CRYOCHEM 2.0 (S. P. Tan & J. S. Kargel 2018) to calculate the fugacities.

CRYOCHEM is a thermodynamic EOS that can deal with phase equilibria involving vapor, liquids, and solids of multicomponent mixtures. Its framework is based on the thermodynamic perturbation theory that calculates the residual molar Helmholtz free energy of the equilibrium phases as a function of density, temperature, and composition. The system pressure, as well as the fugacities, are derived from the free energy. The thermodynamic framework allows it to have transferable pure-component parameters that are derived from pure-component condensation and melting data. The parameters, which represent molecular size and potential energy, are then used to represent the binary mixture through a mixing rule that only has a single adjustable binary-interaction parameter (BIP) to make small corrections to the interaction between unlike molecules. There can only be a constant BIP or a temperature-dependent one for each phase of the mixture, which may be derived to match the binary phase-equilibrium data for accuracy. Fluid mixtures (vapor and liquid) use the same BIP, but solid mixtures of different crystalline structures have their own BIPs. Interested readers are referred to S. P. Tan & J. S. Kargel (2018) for more details about the EOS.

According to the phase rule for a binary mixture in three-phase equilibrium, the degree of freedom of the system is unity and thus a univariant system where only an intensive property is allowed to vary to determine any other intensive properties of the system. Experimentally, the cooling process is carried out by controlling the temperature $T$ to decrease gradually by small steps as mentioned earlier. The other unknown intensive properties to solve are the pressure $P$ where the SLV equilibrium occurs and the corresponding phase compositions $q_1$, $x_1$, and $y_1$ to arrive at the three-phase equilibrium. These four unknowns are to be solved from four simultaneous equations in Equation (3). The compositions of the second component are also fixed as the mole fractions in a phase sum to unity. Therefore, for each temperature set in the experiment, there is only one pressure that satisfies the SLV phase equilibrium, which may be plotted on a $P$–$T$ phase diagram. At the same time, the phase compositions are also obtained, with $q$ and $x$ plotted on the temperature–composition condensed phase diagram as solidus and liquidus, respectively.

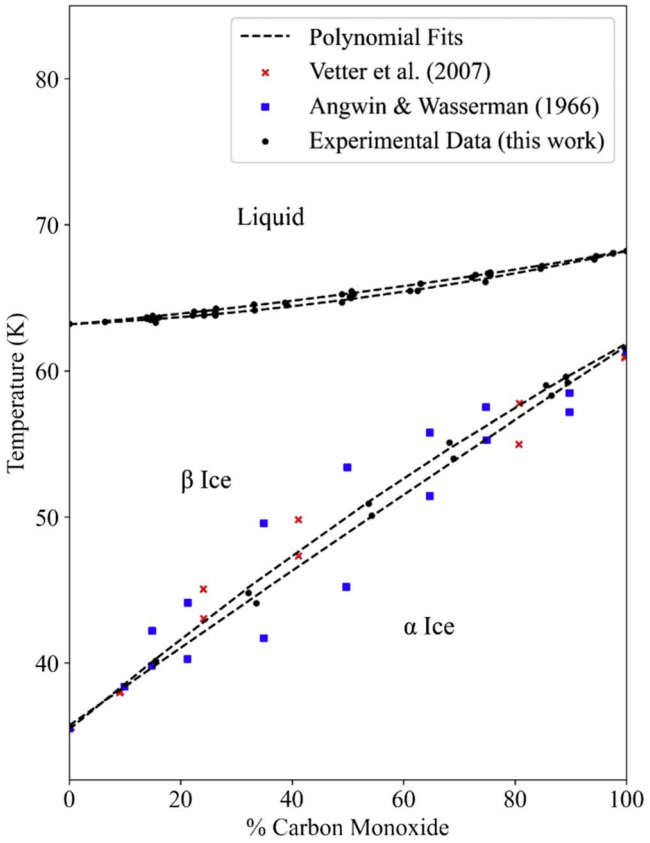


**Figure 5.** $N_2$–CO binary phase diagram. The black scatter points are the experimentally determined phase transition points, while the black dashed lines are polynomial fits. Compositions reported in mole fraction.
(The data used to create this figure are available in the online article.)

As described earlier, it is well known that both $N_2$ and CO exhibit polymorphism with hexagonal crystalline structure at high temperatures and cubic structures at lower temperatures, i.e., $\beta$-solid phase ($S^{\beta}$) and $\alpha$-solid phase ($S^{\alpha}$), respectively. Therefore, to calculate the phase boundaries of the three-phase SSV equilibrium, the liquid L in Equation (3) is replaced by $S^{\alpha}$, while the solid S in the equation is now explicitly labeled as $S^{\beta}$.

Prior to this work, CRYOCHEM 2.0 did not have the parameters for the solid $S^{\alpha}$ but did include the $S^{\beta}$ of both $N_2$ and CO, which were derived earlier (S. P. Tan & J. S. Kargel 2018) by fitting the experimental melting points ($S^{\beta}L$ curve). In this work, the parameters for $S^{\alpha}$ of $N_2$ and CO were derived by fitting the experimental transition points ($S^{\alpha}S^{\beta}$ curve) as detailed in Appendix A.4.

## 3. Results

### 3.1. Experimental Results: Phase Diagram

The experimental data (black points) were collected and added to a temperature-versus-composition phase diagram with the associated polynomial fits (black dashed lines) discussed in Section 2.4 (Figure 5). As mentioned previously, the uncertainty on temperature is ±0.5 K, and the uncertainty on composition is ±1.0%. These data are compared to the literature data (M. Vetter et al. 2007, red crosses; M. J. Angwin & J. Wasserman 1966, blue squares). The alpha–beta ice transition curves from the literature are consistent with the experimental data on the very $N_2$-rich side of the phase diagram, as the upper and lower curves pinch together there. The experimental data are shown to have a smaller coexistence region overall than M. J. Angwin & J. Wasserman (1966) but are closer to the data from M. Vetter et al. (2007).

### 3.2. Comparison to Thermodynamic Model (CRYOCHEM 2.0)

With the EOS parameters for both alpha and beta solids of pure $N_2$ and CO, the alpha–beta transition of binary $N_2$–CO can be calculated using CRYOCHEM EOS, which needs BIPs for both beta-solid and alpha-solid mixtures. The parameters are to be adjusted to fit the experimental data. The parameter for the beta-solid mixture was in fact obtained in our previous work (S. M. Raposa et al. 2022) but needs to be readjusted due to the new set of parameters of beta-solid pure CO as explained in Appendix A.4. The new BIP of the beta-solid mixture is now 0.0092 (see the old one, 0.0162) after fitting over the three-phase SLV data in the same manner as done before (S. M. Raposa et al. 2022). The resulting liquidus–solidus calculations are plotted on the phase diagram in Figure 6(a).

As discussed in the previous section, the EOS needs a BIP for each solid phase and a fluid BIP for the vapor to calculate the $S^{\alpha}S^{\beta}$ coexistence in three-phase SSV equilibrium. While the latter BIP and that of the beta-solid mixture have been previously derived from LV (liquid–vapor) and SLV equilibrium, respectively, the BIP of the alpha-solid mixture still needs to be derived from the SSV equilibrium. Unfortunately, the available SSV data sets in the literature are inconsistent with one another so that two different BIPs are tried here to fit the upper $S^{\alpha}S^{\beta}$ boundary, and the resulting lower boundary is then evaluated. The upper boundary by M. J. Angwin & J. Wasserman (1966; triangles in Figure 6(b)) can be described using a smaller BIP of 0.025, while that of M. Vetter et al. (2007; crosses and plus signs) can be described using a larger BIP of 0.03. However, the resulting phase diagrams can reproduce the corresponding lower boundaries only on the $N_2$-rich and CO-rich ends but not in the region of intermediate compositions. In fact, no BIP values can simultaneously reproduce the upper and lower phase boundaries of a data set satisfactorily. Therefore, CRYOCHEM cannot recommend which data set is more accurate, but qualitatively, the EOS may be seen in Figure 6(b) to be more consistent with data by Vetter et al. in having a wider phase-coexistence region and a closer calculated upper boundary to the current experimental data. This is also reflected by the curve with a BIP of 0.03 on the *P–T* phase diagram in Figure 7, which also shows the approximate range of conditions at Pluto's surface, i.e., 33–55 K and 10–25 $\mu$bar (L. A. Young et al. 2018). For comparison, Triton's surface appears to have a narrower range of temperature and pressure at 35.6–41 K (e.g., A. L. Broadfoot et al. 1989; G. L. Tyler et al. 1989; R. V. Yelle et al. 1991; W. M. Grundy et al. 1993; K. A. Tryka et al. 1993) and 14–19 $\mu$bar (W. B.McKinnon & R. L. Kirk 2014).

Note that the SSV curve on the *P–T* phase diagram borders two regions, i.e., one at higher pressures that may have $S^{\beta}V$ and the other at lower pressures that may have $S^{\alpha}V$ isothermally, or, equivalently, one at lower temperatures that may have $S^{\beta}V$ and the other at higher temperatures that may have $S^{\alpha}V$ isobarically, depending on the composition. Both regions span from the SSV curve to the sublimation curves of $N_2$ and CO, beyond which the phases become all solid or all vapor for any compositions, respectively. Therefore, if the binary $N_2$–CO were present by itself in solid–vapor equilibrium on Pluto's or Triton's surface, it must have beta solid at low temperatures to the left of the SSV curve and alpha solid

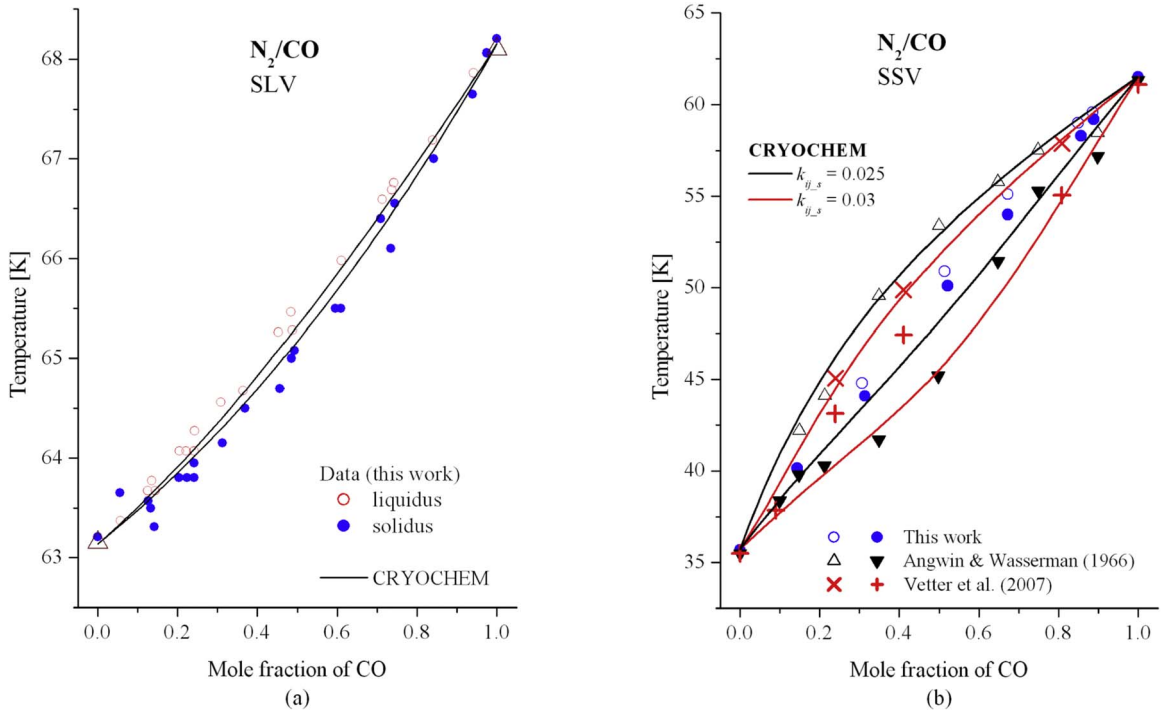


**Figure 6.** CRYOCHEM on the binary $N_2$–CO. (a) Liquidus–solidus pair on a condensed phase diagram obtained by fitting the BIP to SLV *P*–*T* data. (b) Alpha–beta solid phase coexistence at SSV by adjusting the BIP $k_{ij\_s}$ to the experimental upper boundary data.
(The data used to create this figure are available in the online article.)

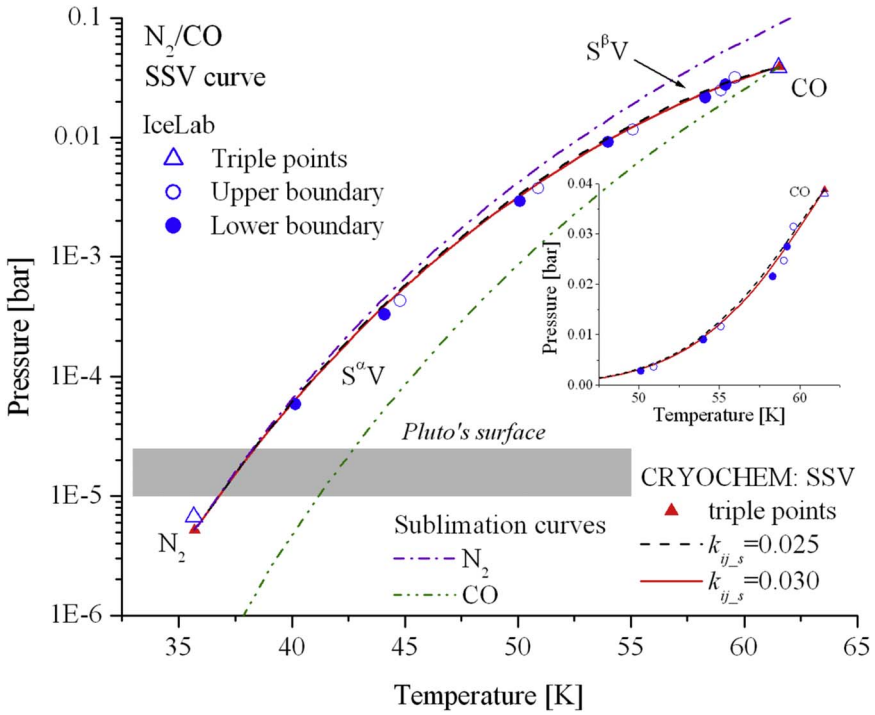


**Figure 7.** *P*–*T* phase diagram showing the SSV curve of binary $N_2$–CO. The experimental conditions at the upper and lower boundaries in Figure 6(b) are plotted as open and filled circles, respectively. The approximate range of conditions at Pluto's surface is shown as a shaded rectangle. Inset: upper portion of the SSV curve in linear scale to make better a comparison between BIP $k_{ij\_s}$ of 0.025 and 0.03 when used in CRYOCHEM. The data set used to create this figure is available (see Figure 6 data).

otherwise, both limited by the sublimation curves where we can still find two-phase SV (solid–vapor) equilibria. It is in contrast with pure $N_2$, where its beta solid is in the high-temperature range above its SSV triple point.

To illustrate the situation described above more clearly, an isobaric phase diagram is given in Appendix A.5. The pressure is chosen such that the resulting diagram can show the equilibrium phases distinctly, particularly for mixtures with

small fractions of CO, such as that on Pluto and Triton. The pressure chosen for the diagram is 20.56 $\mu$bar, where the SSV equilibrium takes place at 38 K. In fact, this pressure is quite high for Triton's surface but reasonable for Pluto's northern summer in the past as pointed out by P. E. Johnson et al. (2021). Since important features of the diagram stay the same if the pressure decreases, the scenarios inferred from the diagram can be generalized to lower pressures. The main point is that the binary $N_2$–CO with a small fraction of CO is in the vapor phase when the pressure and temperature allow SSV equilibrium. Only if it is isobarically cooled down from the SSV temperature will it enter the two-phase $S^{\beta}V$ region and thus the appearance of the beta solid. Further cooling will eventually freeze all vapor into the beta solid. This may help explain why the alpha solid has not been detected so far on Pluto's surface.

Nevertheless, the presence of other components, such as $CH_4$ on Pluto, which is much more abundant than CO, should determine the final type of the solid solution, even though most $CH_4$ must have precipitated in $CH_4$-rich solid at higher elevation (S. P. Tan 2022), as observed in the massive $CH_4$ deposits on the bladed terrains of Tartarus Dorsa (J. M. Moore et al. 2018). This issue is beyond the scope of this paper and is subject to a future investigation.

## 4. Discussion

Overall, the liquidus and solidus curves are straightforward to derive, and the experimental results are consistent with those from CRYOCHEM 2.0. However, the alpha–beta curves remain difficult to produce at cryogenic temperatures, leading to these discrepancies between the various literature works. If this system has narrower coexistence regions, such as derived in this study, this would have implications for Pluto and Triton such that there would be less opportunity for both the beta and alpha phases to be seen together. A larger coexistence region, as seen in M. J. Angwin & J. Wasserman (1966) and M. Vetter et al. (2007), as well as CRYOCHEM 2.0, would allow for these two phases to coexist on the icy surfaces for a larger range of temperatures. In any case, this coexistence region, despite its narrowness, is important to note in the context of planetary surfaces since it is often assumed that only one phase exists without the other (even though that may not always be true).

Temperatures relevant to these phase transitions are present in the outer solar system, particularly in ice giant satellites and trans-Neptunian objects, where one may expect to observe atmospheric (or exospheric) transport moving these species around. Specifically, Pluto's and Triton's surface temperatures (~35–40 K where $N_2$ ice exists and higher in regions without $N_2$) are directly relevant to the SSV curve derived in this study (see full *P–T* profiles for the lower atmospheres of Pluto and Triton in D. P. Hinson et al. 2017; D. F. Strobel & X. Zhu 2017). It was already known that CO and $N_2$ share very similar exospheric dynamics due to their very similar molecular weights and sublimative kinetics (J. K. Steckloff et al. 2022). Thus, locations that favor the condensation of one species would tend to similarly favor the other. Indeed, CO and $N_2$ deposits have been observed to be colocated in Pluto's Sputnik Planitia (T. Bertrand & F. Forget 2016) and across Triton's surface (S. C. Tegler et al. 2019).

While the low pressures at the surfaces of these icy bodies preclude the existence of liquids (regardless of temperature), pressures in the subsurface below ~30 m can exceed the three-phase SLV pressures, allowing for liquids if temperatures allow. Thus, if the observed CO–$N_2$ ice deposits are very thick, liquid pockets could exist below the surface. In particular, $N_2$-rich mixtures would be the first to liquefy due to their lower melting points. Indeed, the observed concentrations on these bodies suggest $N_2$-dominated deposits, making subsurface liquid pockets more likely. Although the temperatures throughout the $N_2$-dominated ice deposit in Sputnik Planitia are too low for liquids to exist (W. B. McKinnon et al. 2016; A. J. Trowbridge et al. 2016), tidal heating within Triton could generate sufficient heat flow to enable liquid melt. Detecting such pockets would require specialized in situ techniques, such as spacecraft-flown ground-penetrating radar.

It is worth noting that the alpha–beta transition of binary $N_2$–CO occurs over a wide temperature range, from ~36 to 60 K, with the exact temperature depending on composition. The New Horizons spacecraft was looking for both alpha and beta nitrogen phases on Pluto. Although only the beta phase of nitrogen was detected, it is plausible that a localized CO-containing nitrogen ice could enable small areas to enter the alpha phase at ~38 K as allowed by the *P–T* phase diagram of the binary mixture. However, it is unclear if any such nitrogen ice with high concentrations of CO (on the order of ~10% at ~38 K as seen in Figure 6(b)) exists anywhere on the surface of Pluto.

## 5. Conclusions

A better understanding of the $N_2$–CO binary mixture is important for the outer solar system, where these materials exist at cryogenic temperatures on and beneath the surface. Specifically, $N_2$ and CO are often found to coexist at Pluto and Triton due to their similar molecular weights and sublimative kinetics. On the surface, they exist generally as ices, but pockets of liquid could be found below the surface as well. This fact has motivated us to get better measurements of the phase boundaries for this binary mixture.

Using a combination of visual inspection and Raman spectroscopy, the locations of the liquidus, solidus, and alpha–beta phase transitions were measured for the $N_2$–CO binary system. Raman has advantages over IR spectroscopy when studying homonuclear diatomic molecules, such as $N_2$. For instance, $N_2$ is Raman-active and IR-inactive, thus absorbing weakly in IR. Additionally, scattering Raman does not require that the beam pass through the sample unscattered, as is the case with transmission spectroscopy.

The liquidus (measured by visual inspection of the first sign of ice in the sample) and the solidus (measured using Raman spectroscopy) were found consistent with the predicted results of the thermodynamic model, CRYOCHEM 2.0. The liquidus occurred at the same place for warming and cooling sequences. However, the solidus was seen to occur 0.4 K colder on the cooling sequence, and thus the data on warming were adopted to account for these supercooling effects.

The colder alpha–beta ice transitions were measured using Raman spectroscopy and compared to CRYOCHEM 2.0 and the literature data (M. J. Angwin & J. Wasserman 1966; M. Vetter et al. 2007). Supercooling effects were observed on these phase transitions (Figure 4), so, as done for the solidus, only the phase transitions that were observed during the warming sequence are reported in the final phase diagram. The experimental data derived in this work show a smaller alpha–beta coexistence region than M. J. Angwin & J. Wasserman

(1966) and M. Vetter et al. (2007). The curves in this work appear to be closer to M. Vetter et al. (2007), though that work only looked at four compositions. The results from CRYOCHEM 2.0 were also consistent with M. Vetter et al. (2007) in both the temperature–composition and *P–T* phase diagrams. Due to the difficulty in measuring these colder alpha–beta transitions, it is still unclear which set of data is most accurate; thus, this is something to be addressed in future works.

Ultimately, it will be important to study the interactions of $N_2$ and CO with $CH_4$, since it is really the combination of these three that shapes the geology of Pluto and Triton over time. In the next stage of this study, we plan to implement this Raman technique with the addition of $CH_4$ to further fill in the literature gaps for phase diagrams of these materials and aid in updating current geophysical models for these planetary bodies.

## Acknowledgments

Portions of this work and laboratory facility were supported by NASA Solar System Workings Program grants 80NSSC21K0168, 80NSSC18K0203, and 80NSSC19K0556. We are also grateful for philanthropic support from the John and Maureen Hendricks Foundation and from Lowell Observatory's Slipher Society.

## Appendix

### *A.1. Raman Composition Derivation Method*

Having an accurate compositional estimate is crucial to building phase diagrams. While Raman spectroscopy has an extensive heritage of estimating compositions, many of the existing methods are not compatible with our laboratory setup or the molecular systems of interest.

In Raman spectroscopy, the relative intensities within a given spectrum are directly proportional to the concentration of each species, the laser power, and the Raman cross section. However, deriving the cross section is nontrivial, and using absolute peak height as a means of quantification is generally ill-advised (M. J. Pelletier 2003; E. Smith & G. Dent 2019) unless the Raman spectrometer has been custom-built to reliably reproduce the spectral height (e.g., J. H. Giles et al. 1999). Because of this, it is generally more common for band ratios to be used when quantifying sample composition (E. Smith & G. Dent 2019). Through a series of tests, we have found that band area ratios, along with a few other pieces of molecular information, can provide us with an accurate reading of our sample compositions.

The following derivation method may be utilized at any temperature/pressure step during the cooling process in an experiment. The Raman spectrometer probes the condensed sample, such that the samples are in the liquid phase, solid phase, or a combination of the two when the composition measurements are done. We do not measure the gas phase above the condensed sample. The compositions for the experiments in this work are derived at the location of the four phase transition points (liquidus, solidus, and the upper and lower alpha–beta ice curves) so that we may later add the exact composition at each phase transition point to the temperature-versus-composition phase diagram. Thus, the composition is determined from single Raman measurements at each of these four points. However, we check the compositions at temperatures above and below the phase transition points, too, to ensure there is consistency among several measurements.

For studies of cryogenic materials in the enclosed cell system, a focal length of 14 cm is used. It should be noted that the Raman spot size is small (~a few millimeters) in comparison to the whole condensed sample shown in Figure 1(c) (15 mm in diameter). During an experiment, the Raman spectrometer is not moved, as it monitors how a local environment is changing during the cooling process. So, the "sample" we observe in these experiments is really that local environment and not any other part of the mixture. Therefore, observing how the whole condensed sample changes in an experiment is not possible with our setup and is beyond the scope of these experiments. This exact procedure is used from experiment to experiment for consistency.

Figure A1 shows examples of vertically offset, background-subtracted spectra cropped to the peaks of CO (Figure A1(A)) and $N_2$ (Figure A1(B)). The background is taken in every experiment just before injecting the sample into the cell. For these experiments, we use the assigned fundamental vibrational peaks known to occur at 2139 $cm^{-1}$ for CO and 2327 $cm^{-1}$ for $N_2$ (A. Anderson et al. 1970), as these peaks fall within our spectral range. This figure shows the experimental data points collected on different days for compositions of 26%, 52%, and 76% CO (scatter points), along with spectra of each pure species, plotted with their corresponding Gaussian fits (black lines). In this instance, these spectra were taken when the samples were still in the liquid phase (for temperatures around

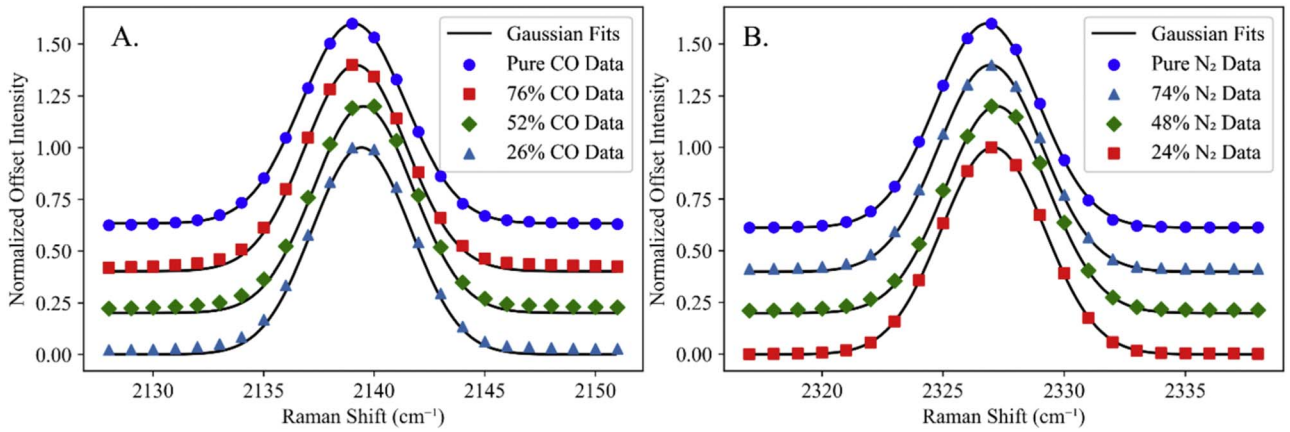


**Figure A1.** Background-subtracted spectra, cropped to show the peaks of (A) CO at 2139 $cm^{-1}$ and (B) $N_2$ at 2327 $cm^{-1}$ for three different compositions (26%, 52%, and 76% CO) along with spectra of each pure species. The experimental data points are plotted with their Gaussian fits (black lines). Note: these spectra were taken on different days, normalized to 1, and vertically offset.

(The data used to create this figure are available in the online article.)

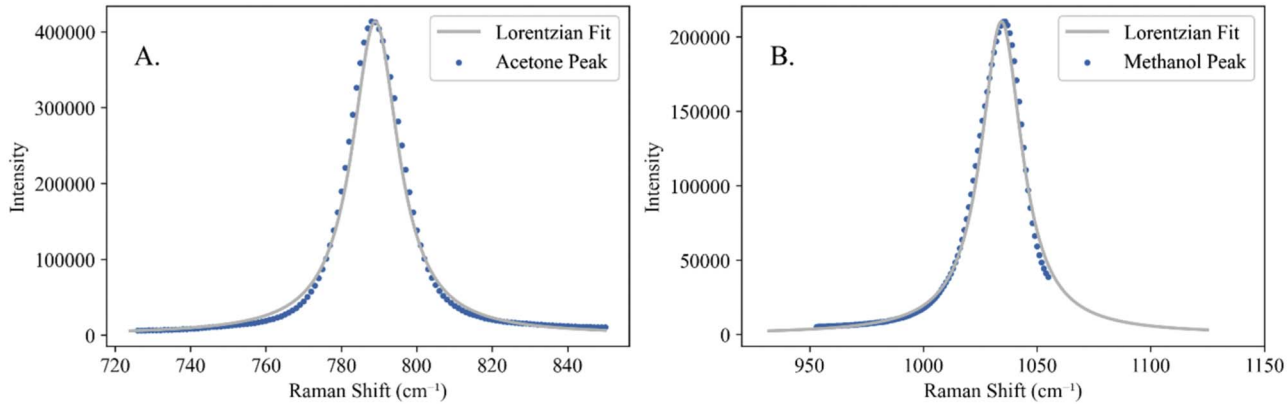


**Figure A2.** Lorentzian fits (gray lines) to (A) acetone and (B) methanol peaks for a mixture of 37.5% acetone, 62.5% methanol (blue scatter points). (The data used to create this figure are available in the online article.)

**Table A1**
Integrated Band Areas of the Gaussian Fits from Figure A1 for CO:$N_2$ Ratios of 26:74, 52:48, and 76:24, along with the Areas of the Pure Spectra

| CO:$N_2$ | 0:100 | 26:74 | 52:48 | 76:24 | 100:0 |
|---|---|---|---|---|---|
| CO area | 0 | 3,210,000 | 3,426,000 | 3,465,000 | 60,530,000 |
| $N_2$ area | 64,240,000 | 9,786,000 | 3,501,000 | 1,194,000 | 0 |

**Note.** The areas are taken from the data before normalization and have an uncertainty of ±0.6%. An exposure time of 15 s was used for the pure spectra.

65–70 K, with pressures in the range ~15,332–33,063 Pa, depending on the spectrum). Table A1 shows the integrated band areas for each peak, taken before normalization, which are used later in the derivation process.

A key idea of this derivation process is that the integrated strength of the Raman band is proportional to the number of moles per unit volume. In other words, it is important to account for how much space each species occupies within the mixture. Ultimately, we want the mole fraction $x$ of species $i$ in a mixture of $i$+$j$+...+$k$ (in the case of binary mixtures, like $N_2$–CO, we would just use the $i$ and $j$ terms, but for ternary mixtures, the $k$ term may be added):

$$x_i = \frac{N_i}{N_i + N_j + N_k + \ldots}. \tag{A1}$$

First, we need to derive an equation for the integrated strength of the Raman band, $R_i$, which is dependent on a few factors. The first is the assumption that $R_i$ scales with the number of moles per unit volume, $N_i$. To get a relative count of the number of moles per unit volume of species $i$ in the mixture ($N_i$) to the pure species, $N_i$ is set as $N_i/N_{i(\text{pure})}$. The next factor is an experimental factor ($E$) that is related to how much material is being sampled, and it depends on the texture of the material and the focus of the beam. This factor affects all species equally. Finally, we need a factor to take into account the Raman response unique to the species, $\sigma_i$, effectively a cross section to Raman scattering of the molecule. Combining this information gives Equation (A2):

$$R_i = E\frac{N_i}{N_{i(\text{pure})}}\,\sigma_i. \tag{A2}$$

Next, the experimental factor, $E$, can be removed by taking a ratio of the integrated strength of the Raman bands for each species. This results in Equation (A3):

$$\frac{R_i}{R_j} = \frac{EN_i\sigma_i N_{j(\text{pure})}}{EN_j\sigma_j N_{i(\text{pure})}} = \frac{N_i\sigma_i N_{j(\text{pure})}}{N_j\sigma_j N_{i(\text{pure})}}. \tag{A3}$$

Another ratio using the Raman bands for the pure species gets rid of the ratio of the cross sections, $\sigma_i/\sigma_j$:

$$\frac{R_{i(\text{pure})}}{R_{j(\text{pure})}} = \frac{\text{EN}_{i(\text{pure})}\sigma_i N_{j(\text{pure})}}{\text{EN}_{j(\text{pure})}\sigma_j N_{i(\text{pure})}} = \frac{\sigma_i}{\sigma_j}. \tag{A4}$$

Now, solve for $N_i/N_j$ by rewriting Equation (A3) to get Equation (A5):

$$\frac{N_i}{N_j} = \frac{R_i\sigma_j N_{i(\text{pure})}}{R_j\sigma_i N_{j(\text{pure})}}. \tag{A5}$$

We need equations for $N_{i(\text{pure})}$ and $N_{j(\text{pure})}$, which is the number of moles per unit volume of the pure species. This is derived by factoring in information about the density ($\rho$) and molar mass ($\mu$) of the pure species. A molar mass of 28.014 g mol$^{-1}$ is used for $N_2$, with 28.010 g mol$^{-1}$ used for CO. Spectra of the pure species were obtained in the liquid phase (Figure A1) at an arbitrary temperature where we know the density. For $N_2$, we used the known liquid density at 69 K, 842.8 kg m$^{-3}$, and for CO, we used the density at 70 K, 842.1 kg m$^{-3}$. Factoring in this information results in Equations (A6) and (A7):

$$N_{i(\text{pure})} = \frac{\rho_{i(\text{pure})}}{\mu_{i(\text{pure})}}, \tag{A6}$$

$$N_{j(\text{pure})} = \frac{\rho_{j(\text{pure})}}{\mu_{j(\text{pure})}}. \tag{A7}$$

Plugging Equations (A4), (A6), and (A7) into Equation (A5) gives the final piece needed to derive the abundance ratio of one species to the other, $N_i/N_j$ . Here, we can plug in the

integrated band areas, such as those derived in Table A1:

$$\frac{N_i}{N_j} = \frac{R_i R_{j(\text{pure})} \rho_{i(\text{pure})} \mu_{j(\text{pure})}}{R_j R_{i(\text{pure})} \rho_{j(\text{pure})} \mu_{i(\text{pure})}}. \quad \text{(A8)}$$

Finally, Equation (A8) can be plugged into Equation (A9) to get the mole fraction of any species:

$$x_i = \frac{1}{1 + \frac{N_j}{N_i} + \frac{N_k}{N_i} + \ldots}. \quad \text{(A9)}$$

This process of deriving Raman compositions may be applied to mixtures beyond binary mixtures, as shown in Equation (A9). However, it is important to note that this method hinges on being able to extract the integrated strength of the bands for the species within a mixture. If the bands overlap each other, this method becomes trickier. Luckily for this work, the $N_2$ and CO bands are well isolated, making it straightforward to calculate the integrated strength for each band. Example code showing our composition derivation method and all of the Raman spectra used in these experiments is provided in Supplementary Materials.

Several factors could contribute to compositional uncertainty. The first is a spectrometer performance that has noise and could drift over time. We conducted a test in which we held a fixed liquid composition of ~50:50 $N_2$:CO at the same temperature for just over 2 hr, taking Raman spectra every 10–15 minutes. This test showed that the integrated band areas appear to drift over time (plots are provided in Supplemental Materials). This could be because the laser power drifts or because the texture of the material is evolving, so the spectrometer is sampling more or less material. However, when we derive the compositions, we take a ratio of the integrated band strengths, and the ratios are not affected by this drift, as shown in a plot of the derived compositions over the 2 hr (Supplemental Materials), though they do still show low-level scatter from noise in the spectra. We further checked the effect of spectral noise by adding artificial noise to a spectrum, deriving the composition, then adding different noise and rederiving the composition, etc., in a Monte Carlo sense. The effect on derived compositions was negligible for this test as well. Another factor that contributes to the uncertainty is the fits we make to the data (as shown in Figure A1). However, the largest uncertainty in the fit parameters to the data was 0.6%, with the rest falling below this value. To ensure we have accounted for all these small sources of error, plus any additional systematic errors, we are reporting an error of ±1.0% of the measured compositions.

### A.2. Testing Validation of Raman Composition Derivation Method

The Raman composition derivation method was tested for accuracy by taking Raman spectra of known molar abundances of acetone and methanol at room temperature. To get the desired molar abundances, we mixed based on volume. For a total volume of 15 ml ($v_a$+$v_m$ = 15 ml) and desired molar fractions of acetone and methanol, $x_a$ and $x_m$, respectively, we set $c = (x_a/x_m)(\mu_m/\mu_a)(\rho_a/\rho_m)$, where the molar mass, $\mu_a$, of acetone is 58.08 g mol$^{-1}$ and the molar mass of methanol, $\mu_m$, is 32.04 g mol$^{-1}$. The densities used for acetone and methanol at room temperature (23°C), $\rho_a$ and $\rho_m$, respectively, are 0.7846 g cm$^{-3}$ for acetone and 0.7910 g cm$^{-3}$ for methanol. We computed the volume needed for a certain molar abundance to be $v_a = 15^* c/(1+c)$. The target volumes of each species were added to a beaker using a pipette with 0.1 ml gradations, stirred, and then deposited into a small cylindrical glass bottle that was placed inside the Raman apparatus. For tests at room temperature, a focal length of 1 cm was used, enabling us to block out room light from contaminating the spectra. Though the focal length is different than the focal length used for the cryogenic experiments and thus probes a different volume of material, this does not change the results for relative abundances. We measured abundances at every eighth (0:8, 1:7, 2:6, 3:5, 4:4, etc.) so that we recorded Raman spectra of seven total mixtures, plus spectra of pure acetone and pure methanol.

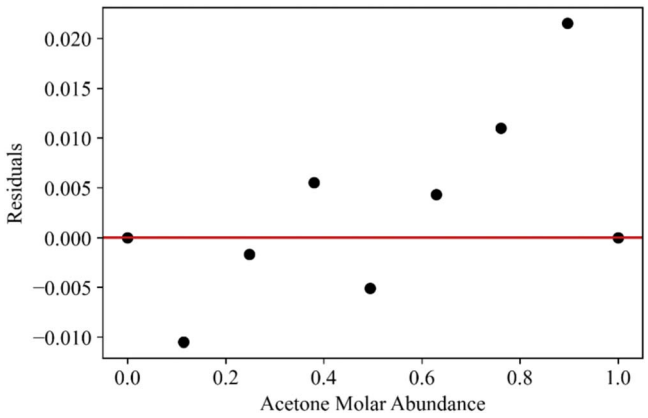


**Figure A3.** Residuals of actual derived molar abundances using the Raman composition derivation method compared to expected molar abundance values. The scatter appears to be dominated by our ability to mix the target composition owing to the 0.1 ml resolution of our pipette.
(The data used to create this figure are available in the online article.)

When rederiving the molar abundances from the Raman data, we used the peaks of acetone and methanol at 789 cm$^{-1}$ and 1034 cm$^{-1}$, respectively. These are the most isolated peaks in the spectral range and thus the easiest to measure. There was some slight overlap in an acetone peak near the methanol peak. To get rid of this, we first fit a Lorentzian to the pure acetone peak. It should be noted that a Lorentzian fit was the best match for both the acetone and methanol peaks, whereas a Gaussian fit worked best for the $N_2$ and CO peaks. Next, we determined what factor this Lorentzian peak could be multiplied by to best match the acetone peak in the spectrum of the mixture. Then, we multiplied the spectrum of the mixture by this factor to reduce the intensity in the acetone peak. Once the acetone peak was removed to our satisfaction, we fit Lorentzian peaks to both the acetone and methanol mixture peaks (Figure A2). The areas from these fitted peaks were used in conjunction with the areas of the pure peaks in the Raman composition derivation method described previously to obtain the actual molar abundances of the seven mixtures. The residuals from these seven mixtures compared to the expected values are shown in Figure A3.

### A.3. Sample Appearance

The appearance of the $N_2$–CO samples follows general trends on each side of the phase diagram. Figure A4 shows an example of a CO-rich mixture (here, the sample is 88% CO, 12% $N_2$). On the CO-rich side of the phase diagram, the sample generally appears more transparent, with less scattering at the liquidus, or the first sign of ice (Figure A4(A)). Once the sample becomes entirely ice, we see two different regions

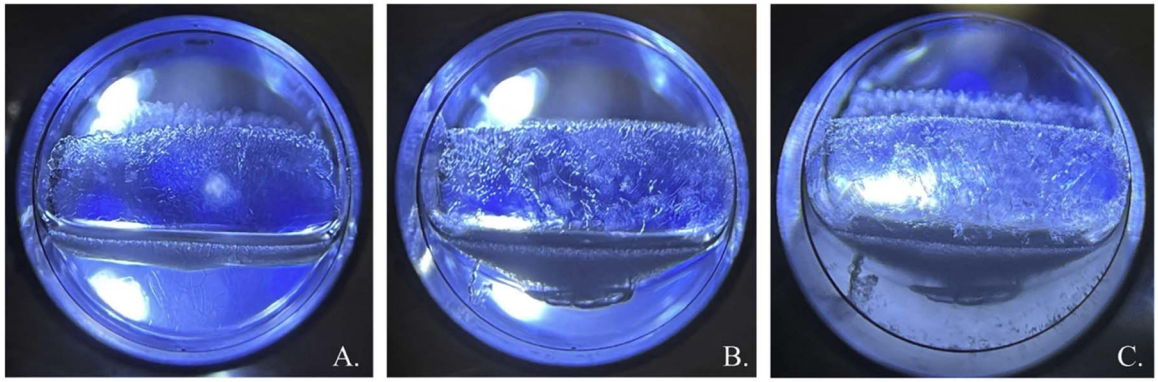


**Figure A4.** Example of the general appearance for a CO-rich sample (in this case, the sample is 88% CO, 12% $N_2$) (A) at the first sign of ice, or the liquidus; (B) at the region between the solidus and the $\alpha$–$\beta$ phase transition; and (C) after crossing through the $\alpha$–$\beta$ phase transition.

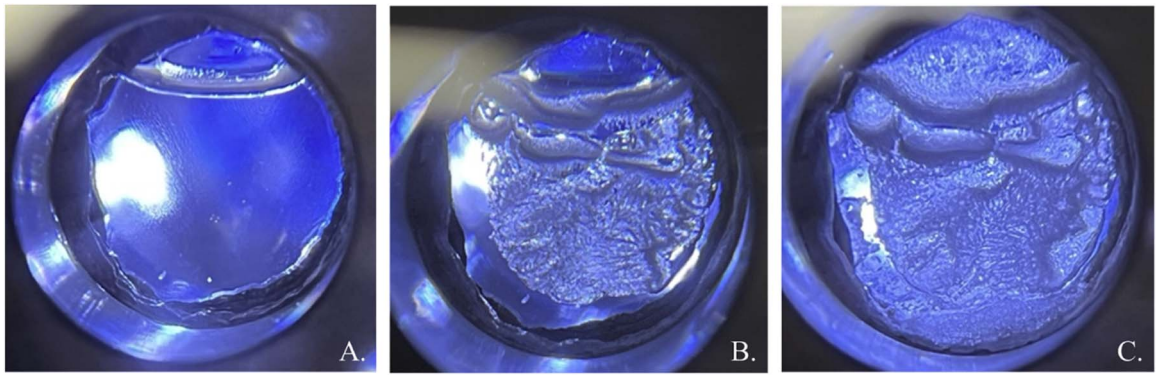


**Figure A5.** Example of the general appearance for a $N_2$-rich sample (in this case, the sample is 22% CO, 78% $N_2$) (A) at the first sign of ice, or the liquidus; (B) at the region between the solidus and the $\alpha$–$\beta$ phase transition; and (C) after crossing through the $\alpha$–$\beta$ phase transition.

(Figure A4(B)). The top region is strongly scattering, while the bottom remains less scattering and more transparent. Upon further cooling through the $\alpha$–$\beta$ phase transition, the bottom part transitions from being transparent to more scattering as well (Figure A4(C)), perhaps due to scattering by voids that may be created as the sample becomes denser while transitioning to the $\alpha$-ice phase.

Figure A5 shows an example of the evolution of a $N_2$-rich mixture (22% CO, 78% $N_2$). Similarly to the CO-rich side of the phase diagram, the liquidus appears as transparent ice (Figure A5(A)). After crossing through the solidus, the appearance of the ice is fairly different from that of the CO-rich mixture. Like the other side of the phase diagram, when freezing the sample, the liquid appears to shrink and create voids. In these voids, we may get a mix of ice plus low-pressure vapor pockets. This creates the appearance of different pockets of material, as displayed in Figure A5(B). Despite this difference in appearance, the sample is displaying similar trends to the CO-rich side. In this subsolidus region, the bottom left part of the sample is transparent (Figure A5(B)). Like on the CO-rich side, this region becomes more scattering when transitioning to $\alpha$-ice (Figure A5(C)).

### *A.4. CRYOCHEM Solid Parameters*

The CRYOCHEM parameters of the $\alpha$-solid phase of pure $N_2$ and pure CO are fitted to the experimental SS phase transition $S^{\alpha}S^{\beta}$ points available in the literature (J. R. Brookeman & T. A. Scott 1973; E. Fukushima et al. 1977). The fits are plotted on the *P–T* phase diagrams as shown in Figure A6.

In deriving the $\alpha$-solid parameters of pure CO from its $S^{\alpha}S^{\beta}$ curve, it turned out that the old $\beta$-solid parameters need to be refitted from the melting $S^{\beta}L$ curve to give a good overall representation as that in Figure A6. The new parameters of the $\beta$-solid phase were then used for rederiving the BIP $k_{ij-s\beta}$ in the SLV equilibrium, the accuracy of which was found to be similar to the old one published in S. M. Raposa et al. (2022) as shown in Figure A7 below. Table A2 lists the solid parameters of pure $N_2$ and CO.

The accuracy of the experimental data and calculations applying the parameters may be evaluated using the literature data of the $S^{\alpha}S^{\beta}V$ triple points as listed in Table A3.

### *A.5. Isobaric Phase Diagram*

Figure A8 below shows an isobaric phase diagram of binary $N_2$–CO at 20.56 $\mu$bar, where the SSV temperature is 38 K and the equilibrium CO mole fractions are 0.0191, 0.0641, and 0.1144 in vapor, beta solid, and alpha solid, respectively. The isobaric diagram is accompanied by the corresponding *P–T* diagram, which is a portion of Figure 7 in a small temperature range of 36–43 K in the vicinity of the SSV curve.

The isobaric phase diagram shows three two-phase regions, i.e., $VS^{\alpha}$ above the three-phase VSS line (>38 K) and $VS^{\beta}$ and $S^{\alpha}S^{\beta}$ below the three-phase line (<38 K). We can only find vapor–solid equilibria at 38–42.36 K for $VS^{\alpha}$ and at 37.92–38 K for $VS^{\beta}$. The limits of 42.36 and 37.92 K are the sublimation temperatures at 20.56 $\mu$bar of pure CO and $N_2$, beyond which the equilibrium phase at the pressure is all vapor and all solid, respectively. Therefore, if we increase the temperature isobarically from the SSV

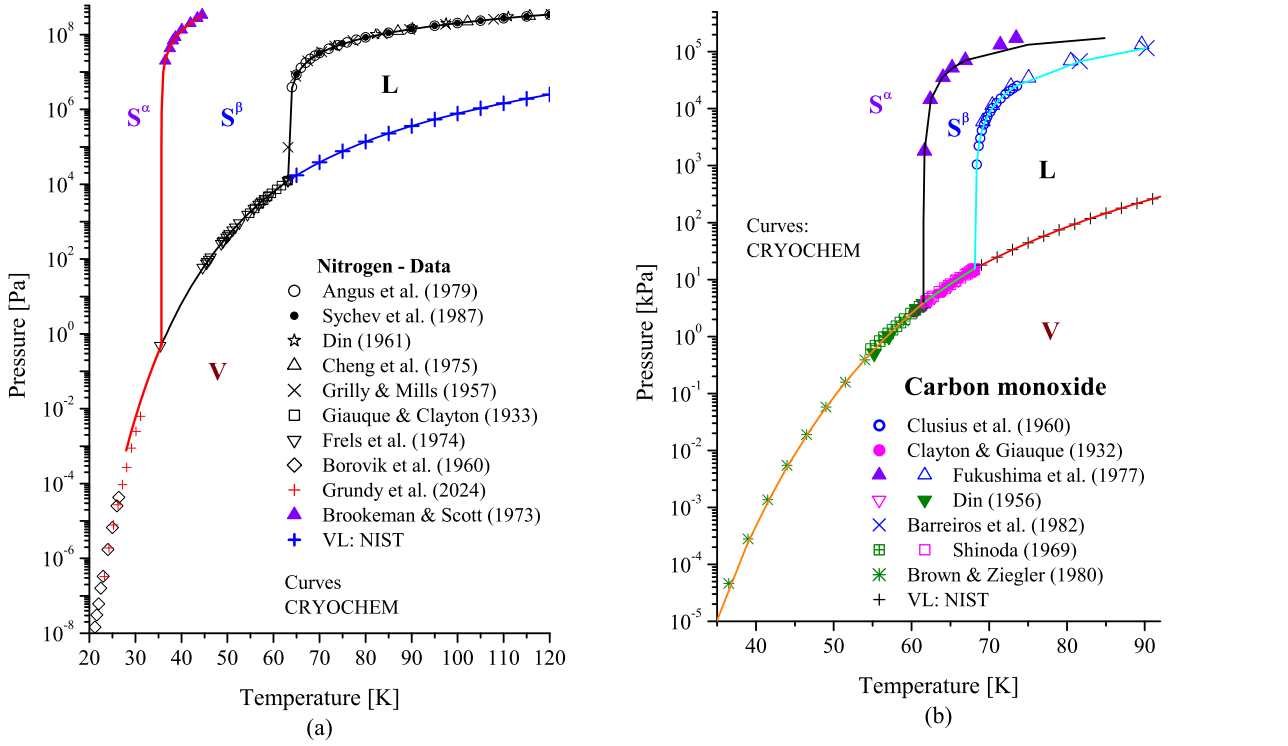


**Figure A6.** Phase diagrams of (a) pure N2 and (b) pure CO. All data sources are included in the reference list.
(The data used to create this figure are available in the online article.)

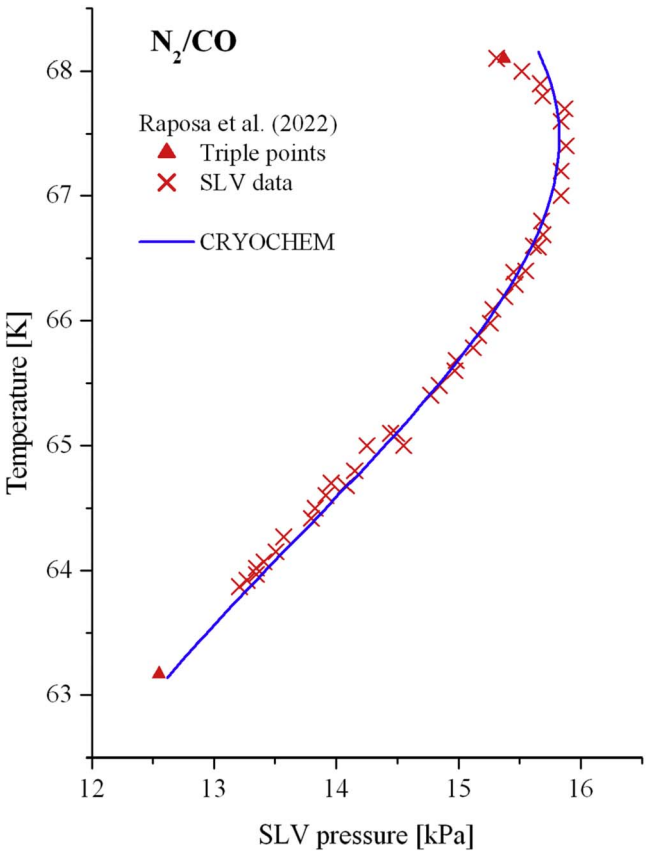


**Figure A7.** SLV *P*–*T* phase diagrams of binary $N_2$–CO with a new curve by CRYOCHEM 2.0 using the new set of parameters of beta-solid CO and new $k_{ij-s} = 0.0092$. The data set used to create this figure is available (see Figure 6 data).

temperature 38 K, any compositions between 0.0191 and 0.1144 CO will enter the $VS^{\alpha}$ region. Increasing the temperature further will sublime all solid phase into vapor. On the other hand, if we lower the temperature isobarically from 38 K, the compositions between 0.0191 and 0.064 1 CO will enter $VS^{\beta}$, while those between 0.0641 and 0.1144 CO will enter the SS region as the vapor vanishes. Decreasing the temperature further will freeze all vapor to beta solid for the former and transform all solid into alpha solid for the latter.

At 38 K, any compositions with CO more than 0.1144 are in alpha solid, and only by increasing the temperature isobarically will they have two-phase $VS^{\alpha}$ equilibrium. On the other hand, any compositions with CO less than 0.0191 are in the vapor phase, and only by cooling isobarically will they have two-phase $VS^{\beta}$ equilibrium. With a very small fraction of CO relative to $N_2$, such as that on Pluto and Triton, this latter scenario is the most relevant.

The features of the isobaric phase diagram shown in Figure A8 will be preserved if the pressure is lowered to a more realistic value of the present surface condition on Pluto or Triton. The predictable changes will be the SSV and the sublimation of $N_2$ and CO, which all drop to lower temperatures, while the bottom tip of the SS region practically stays at a temperature near the triple SSV point of $N_2$ (~35.7 K). These changes will make the phase diagram so crowded at small CO fractions that it becomes harder to see the phase-equilibrium regions distinctly when it is presented in the entire range of composition. This is the very reason for choosing a higher pressure of 20.56 bars in the first place, but as the important features stay the same at lower pressures, the description discussed above, except for the numbers, can also be qualitatively generalized to include conditions at lower pressures.

**Table A2**
CRYOCHEM Solid Parameters of Pure $N_2$ and CO

| | $\alpha$-solid Phase | $\beta$-solid Phase[a] |
|---|---|---|
| Nitrogen | $m_{s\alpha} = 1.19997943$ $\varepsilon_{s\alpha}/k_B = 88.51215401$ [K] $\sigma_{s\alpha} = 3.43053843$ $-2.000928211 \times 10^{-4}T$ | $m_{s\beta} = 1.04252051$ $\varepsilon_{s\beta}/k_B = 97.05008999$ [K] $\sigma_{s\beta} = 3.59457758$ $-7.03475096 \times 10^{-4}T$ |
| Carbon monoxide | $m_{s\alpha} = 1.62999029$ $\varepsilon_{s\alpha}/k_B = 81.99984298$ [K] $\sigma_{s\alpha} = 3.22971867$ $-2.452427586 \times 10^{-3}T$ | $m_{s\beta} = 1.11999489$ $\varepsilon_{s\beta}/k_B = 99.60937412$ [K] $\sigma_{s\beta} = 3.54229573$ $-2.20704538 \times 10^{-4}T$ |
| $N_2$+CO | $k_{ij\_s\alpha} = 0.025$ or 0.03[b] | $k_{ij-s\beta} = 0.0092$ |

**Notes.**
[a] For $\beta$-solid nitrogen, the parameter set is from S. P. Tan & J. S. Kargel (2018).
[b] See Figure 6(b) for the performance of each BIP.

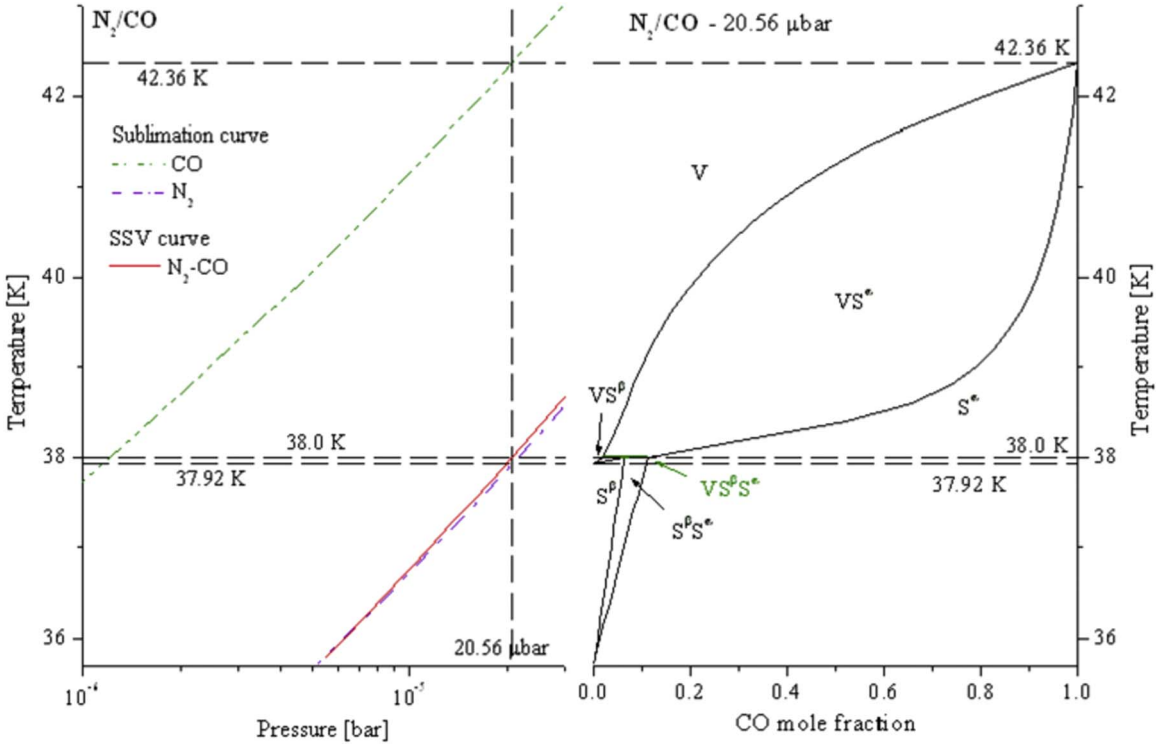


**Figure A8.** Isobaric phase diagram of $N_2$–CO at 20.56 $\mu$bar (right-hand panel) along with its corresponding *P*–*T* phase diagram (left-hand panel). All curves were calculated using CRYOCHEM.

(The data used to create this figure are available in the online article.)

**Table A3**
$S^{\alpha}S^{\beta}V$ Triple Points: Comparison of Experimental Data and CRYOCHEM Calculations Applying the Parameters in Table A2

| | Nitrogen | Carbon Monoxide |
|---|---|---|
| Experiment (this work) | 35.68 K, 0.667 Pa | 61.52 K, 3.81 kPa |
| CRYOCHEM | 35.71 K, 0.521 Pa | 61.55 K, 3.88 kPa |
| Literature data | 35.4 K, 0.484 Pa (S. Aoyama & E. Kanda 1934); 35.5 K, 0.467 Pa (F. Din 1961); 35.61 K (J. R. Brookeman & T. A. Scott 1973) | 61.55 K, 3.75 kPa (A. S. Leah 1956); 61.584/6 K, 3.74 kPa (J. A. Morrison et al. 1968) |

## ORCID iDs

Shaelyn M. Raposa https://orcid.org/0000-0002-8691-5214
Sugata P. Tan https://orcid.org/0000-0003-2049-3706
William M. Grundy https://orcid.org/0000-0002-8296-6540
Jordan K. Steckloff https://orcid.org/0000-0002-1717-2226
Jennifer Hanley https://orcid.org/0000-0002-0801-7654
Stephen C. Tegler https://orcid.org/0000-0002-6794-495X
Anna E. Engle https://orcid.org/0000-0002-7894-7056
Cecilia L. Thieberger https://orcid.org/0000-0001-7399-434X
Gerrick E. Lindberg https://orcid.org/0000-0002-5292-4200

## References

Ahrens, C. J., Grundy, W. M., Mandt, K. E., et al. 2018, Recent Advancements and Motivations of Simulated Pluto Experiments, SSRv, 214, 130
Anderson, A., Sun, T. S., & Donkersloot, M. C. A. 1970, Raman Spectra and Lattice Dynamics of the $\alpha$ Phases of Nitrogen and Carbon Monoxide Crystals, CaJPh, 48, 2265
Angus, S, Reuck, K. M., & Armstrong, B 1979, Nitrogen, IUPAC Chemical Data Ser. 20 (Oxford: Pergamon Press), 1
Angwin, M. J., & Wasserman, J. 1966, Nitrogen–Carbon Monoxide Phase Diagram, JChPh, 44, 417
Aoyama, S., & Kanda, E. 1934, Vapor pressures of solid O2 and N2, J. Chem. Soc. Japan, 55, 23
Barreiros, S. F., da Ponte, M. N., Calado, J. C., et al. 1982, The Equation of State and Thermodynamic Properties of Liquid Carbon Monoxide, Advances in Cryogenic Engineering (New York: Springer)
Barrett, C. S., & Meyer, L. 1965, Phase Diagram of Argon–Carbon Monoxide, JChPh, 43, 3502
Bertrand, T., & Forget, F. 2016, Observed Glacier and Volatile Distribution on Pluto from Atmosphere-topography Processes, Natur, 540, 86
Borovik, E. S., Grishin, S. F., & Grishina, E. Y. 1960, The Vapor Pressure of Nitrogen and Hydrogen at Low Pressures, SPTP, 5, 506
Broadfoot, A. L., Atreya, S. K., Bertaux, J. L., et al. 1989, Ultraviolet spectrometer observations of Neptune and Triton, Sci, 246, 1459
Brookeman, J. R., & Scott, T. A. 1973, NQR Study of the $\alpha$-$\beta$ Ordering Transition in Solid Nitrogen as a Function of Pressure, JLTP, 12, 491
Brown, G. N., Jr., & Ziegler, W. T. 1980, Vapor pressure and heats of vaporization and sublimation of liquids and solids of interest in cryogenics below 1-atm pressure, in Advances in Cryogenic Engineering, Vol. 35 A, ed. K. D. Timmerhaus & H. A. Snyder (Boston, MA: Springer), 662
Cheng, V. M., Daniels, W. B., & Crawford, R. K. 1975, Melting Parameters of Methane and Nitrogen from 0 to 10 kbar, PhRvB, 11, 3972

Clayton, J. O., & Giauque, W. F. 1932, The Heat Capacity and Entropy of Carbon Monoxide: Heat Of Vaporization. Vapor Pressures Of Solid And Liquid. Free Energy To 5000 K From Spectroscopic Data, JAChS, 54, 2610
Clusius, K., Piesbergen, U., & Varde, E. 1960, Ergebnisse der Tieftemperaturforschung XXXIII. Die Schmelzkurve von Kohlenoxyd bis 250 Atm. und sein Volumensprung am Schmelzpunkt, Helvetica Chimica Acta, 43, 2059
Dantzig, J. A., & Rappaz, M. 2009, Solidification (Lausanne: EPFL Press)
Din, F 1956, Thermodynamic Diagrams and Functions and Their Preparation, Thermodynamic Functions of Gases, Vol. 1 (London: Butterworths Scientific Publications)
Din, F. 1961, Thermodynamic Functions of Gases, Vol. 3 (London: Butterworths Scientific Publications)
Engle, A. E., Hanley, J., Dustrud, S., et al. 2021, Phase Diagram for the Methane-ethane system and its implications for Titan's lakes, PSJ, 2, 118
Ewing, G. E. 1962, Infrared Spectra of Liquid and Solid Carbon Monoxide, JChPh, 37, 2250
Frels, W., Smith, D. R., & Ashworth, T. 1974, Vapour Pressure of Nitrogen below the Triple Point, Cryo, 14, 3
Fukushima, E., Gibson, A. A. V., & Scott, T. A. 1977, Pressure Dependence of the Melting and $\alpha$-$\beta$ Phase Transition Temperatures of Carbon Monoxide, JLTP, 28, 157
Giauque, W. F., & Clayton, J. O. 1933, The Heat Capacity and Entropy of Nitrogen. Heat of Vaporization. Vapor Pressures of Solid and Liquid. The Reaction 1/2 N2 + 1/2 O2 = NO from Spectroscopic Data, JAChS, 55, 4875
Giles, J. H., Gilmore, D. A., & Denton, M. B. 1999, Quantitative Analysis Using Raman Spectroscopy without Spectral Standardization, JRSp, 30, 767
Grilly, E. R., & Mills, R. L. 1957, Volume Change on Melting of $N_2$ up to 3500 kg/cm$^2$, PhRv, 105, 1140
Grundy, W. M., Morrison, S. J., Bovyn, M. J., Tegler, S. C., & Cornelison, D. M. 2011, Remote Sensing D/H Ratios in Methane Ice: Temperature-dependent Absorption Coefficients of CH3D in Methane Ice and in Nitrogen Ice, Icar, 212, 941
Grundy, W. M., Binzel, R. P., Buratti, B. J., et al. 2016, Surface Compositions Across Pluto and Charon, Sci, 351, aad9189
Grundy, W. M., Schmitt, B., & Quirico, E. 1993, The Temperature-dependent Spectra of $\alpha$ and $\beta$ Nitrogen ice with Application to Triton, Icar, 105, 254
Grundy, W. M., Tegler, S. C., Steckloff, J. K., et al. 2024, Laboratory Measurement of Volatile Ice Vapor Pressures with a Quartz Crystal Microbalance, Icar, 410, 115767
Hinson, D. P., Linscott, I. R., Young, L. A., et al. 2017, Radio Occultation Measurements of Pluto's Neutral Atmosphere with New Horizons, Icar, 290, 96
Johnson, P. E., Young, L. A., Protopapa, S., et al. 2021, Modeling Pluto's Minimum Pressure: Implications for Haze Production, Icar, 356, 114070
Leah, A. S. 1956, Carbon Monoxide, in Thermodynamic Functions of Gases, Vol. 1, ed. F. Din (London: Butterworths Scientific Publications), 165
Loveland, R. J., Le Comber, P. G., & Spear, W. E. 1972, Charge Transport in the Diatomic Molecular Solids and Liquids: N2, O2, and CO, PhRvB, 6, 3121
McKinnon, W. B., & Kirk, R. L. 2014, Triton, in Encyclopedia of the Solar System, ed. T. Johnson (3rd ed.; Amsterdam: Elsevier), 861
McKinnon, W. B., Nimmo, F., Wong, T., et al. 2016, Convection in a Volatile Nitrogen-ice-rich Layer Drives Pluto's Geological Vigour, Natur, 534, 82
Moore, J. M., & Howard, A. D. 2021, The Landscapes of Pluto as Witness to Climate Evolution, in The Pluto System After New Horizons, ed. S. A. Stern, J. M. Moore, W. M. Grundy, L. A. Young, & R. P. Binzel (Tucson, AZ: Univ. Arizona Press), 105
Moore, J. M., Howard, A. D., Umurhan, O. M., et al. 2018, Bladed Terrain on Pluto: Possible Origins and Evolution, Icar, 300, 129
Morrison, J. A., Newsham, D. M. T., & Weir, R. D. 1968, Equilibrium Vapour Pressures of Carbon Monoxide+ Nitrogen Solid Solutions, Transactions of the Faraday Society, 64, 1461
Pangilinan, G., Guelachvili, G., Sooryakumar, R., Rao, K. N., & Tipping, R. H. 1989, Raman Study of the $\alpha \rightarrow \beta$ Structural Phase Transition of Solid N2, PhRvB, 39, 2522
Pelletier, M. J. 2003, Quantitative Analysis Using Raman Spectrometry, ApSpe, 57, 20A
Protopapa, S., Grundy, W. M., Reuter, D. C., et al. 2017, Pluto's Global Surface Composition Through Pixel-by-pixel Hapke Modeling of New Horizons Ralph/LEISA data, Icar, 287, 218
Quirico, E., Doute, S., Schmitt, B., et al. 1999, Composition, Physical State, and Distribution of ices at the Surface of Triton, Icar, 139, 159
Raposa, S. M., Tan, S. P., Grundy, W. M., et al. 2022, Non-isoplethic Measurement on the Solid-liquid-vapor Equilibrium of Binary Mixtures at Cryogenic Temperatures, JChPh, 157, 064201
Ruhemann, M., Lichter, A., & Komarow, P. 1935, Zustandsdiagramme Niedrig Schmelzender Gemische: 2 Das Schmelzdiagramm Sauerstoff-stickstoff und das Zustandsdiagramm Stickstoff-kohlenoxyd, Phys. Z. Sowjetunion, 8, 326
Schmitt, B., Philippe, S., Grundy, W. M., et al. 2017, Physical State and Distribution of Materials at the Surface of Pluto from New Horizons LEISA Imaging Spectrometer, Icar, 287, 229
Scott, T. A. 1976, Solid and Liquid Nitrogen, PhR, 27, 89
Shinoda, T. 1969, Vapor Pressure of Carbon Monoxide in Condensed Phases, Bull. Chem. Soc. Jpn., 42, 2815
Smith, E., & Dent, G. 2019, Modern Raman Spectroscopy: A Practical Approach (New York: Wiley)
Steckloff, J. K., Goldstein, D., Trafton, L., Varghese, P., & Prem, P. 2022, Exosphere-mediated Migration of Volatile Species on airless Bodies Across the Solar System, Icar, 384, 115092
Strobel, D. F., & Zhu, X. 2017, Comparative Planetary Nitrogen Atmospheres: Density and Thermal Structures of Pluto and Triton, Icar, 291, 55
Sychev, V. V., Vasserman, A.A., Kozlov, A. D., et al. 1987, Thermodynamic Properties of Nitrogen, National Standard Reference Data Service of the USSR (Boca Raton, FL: CRC Press)
Tan, S. P. 2022, Low-pressure and Low-temperature Phase Equilibria Applied to Pluto's Lower Atmosphere, MNRAS, 515, 1690
Tan, S. P., & Kargel, J. S. 2018, Solid-phase Equilibria on Pluto's Surface, MNRAS, 474, 4254
Tegler, S. C., Cornelison, D. M., Grundy, W. M., et al. 2010, Methane and Nitrogen Abundances on Pluto and Eris, ApJ, 725, 1296
Tegler, S. C., Grundy, W. M., Olkin, C. B., et al. 2012, Ice Mineralogy Across and into the surfaces of Pluto, Triton, and Eris, ApJ, 751, 76
Tegler, S. C., Stufflebeam, T. D., Grundy, W. M., et al. 2019, A New Two-molecule Combination Band as a Diagnostic of Carbon Monoxide Diluted in Nitrogen Ice on Triton, AJ, 158, 17
Trowbridge, A. J., Melosh, H. J., Steckloff, J. K., & Freed, A. M. 2016, Vigorous Convection as the Explanation for Pluto's Polygonal Terrain, Natur, 534, 79
Tryka, K. A., Brown, R. H., Anicich, V., Cruikshank, D. P., & Owen, T. C. 1993, Spectroscopic determination of the phase Composition and Temperature of Nitrogen ice on Triton, Sci, 261, 751
Turc, C., Perrin, B., Ouillon, R., & Ranson, P. 1992, Effect of Orientational and Substitutional Disorders on the $N_2$ Vibrational Exciton in N2/CO Mixed Crystals, CP, 161, 39
Tyler, G. L., Sweetnam, D. N., Anderson, J. D., et al. 1989, Voyager Radio Science Observations of Neptune and Triton, Sci, 246, 1466
Verschoyle, T. T. H. 1931, The Ternary System Carbon Monoxide-nitrogen-hydrogen and the Component Binary Systems Between Temperatures of -185 and -215 C., and Between Pressures of 0 and 225 atm, RSPTA, 230, 189
Vetter, M., Jodl, H.-J., & Brodyanski, A. 2007, From Optical Spectra to Phase Diagrams–The Binary Mixture $N_2$–CO, LTP, 33, 1052
Yelle, R. V., Lunine, J. I., & Hunten, D. M. 1991, Energy Balance and Plume Dynamics in Triton's Lower Atmosphere, Icar, 89, 347
Young, Leslie A., Kammer, Joshua A., Steffl, Andrew J., et al. 2018, Structure and Composition of Pluto's Atmosphere from the New Horizons Solar Ultraviolet Occultation, Icarus, 300, 174